JGR Solid Earth

RESEARCH ARTICLE
10.1029/2022JB024228

Ambient-Noise Tomography of the Ligurian-Provence Basin Using the AlpArray Onshore-Offshore Network: Insights for the Oceanic Domain Structure

A. Nouibat[1], L. Stehly[1], A. Paul[1], S. Schwartz[1], Y. Rolland[1,2], T. Dumont[1], W. C. Crawford[3], R. Brossier[1], and Cifalps Team, and AlpArray Working Group[4]

[1]Univ. Grenoble Alpes, Univ. Savoie Mont Blanc, CNRS, IRD, UGE, ISTerre, Grenoble, France, [2]Univ. Savoie Mont Blanc, CNRS, UMR 5204, EDYTEM, Le Bourget-du-Lac, France, [3]Institut de Physique du Globe de Paris, Sorbonne Paris Cité, Paris, France, [4]See Appendix A

Key Points:

- Efficient processing scheme to remove transients and reduce tilt and compliance from continuous ambient noise recorded by ocean-bottom seismometers (OBSs)
- Computation of iterative correlations between OBSs based on a virtual reconstruction of the Rayleigh waves
- Thin, anomalous oceanic crust with gabbroic intrusions evidenced in the basin axis from a joint interpretation of V_s and V_p models

Supporting Information:

Supporting Information may be found in the online version of this article.

Correspondence to:

A. Nouibat,
ahmed.nouibat@univ-grenoble-alpes.fr

Citation:

Nouibat, A., Stehly, L., Paul, A., Schwartz, S., Rolland, Y., Dumont, T., et al. (2022). Ambient-noise tomography of the Ligurian-Provence basin using the AlpArray onshore-offshore network: Insights for the oceanic domain structure. *Journal of Geophysical Research: Solid Earth*, *127*, e2022JB024228. https://doi.org/10.1029/2022JB024228

Received 15 FEB 2022
Accepted 5 JUL 2022

Abstract We derive a three-dimensional shear-wave velocity model of the Ligurian-Provence back-arc basin (Northwestern Mediterranean Sea) using ocean-bottom seismometers (AlpArray OBSs) and land stations from permanent and temporary seismic networks. The quality of OBS continuous records is enhanced by a specific processing that reduces instrumental and seabed-induced noises (transients, tilt, compliance). To further improve the resolution of ambient-noise tomography in the offshore area, we compute the Rayleigh-wave part of the Green functions for OBS-OBS pairs by using onshore stations as virtual sources. 2-D group-velocity maps and their uncertainties are computed in the 4–150 s period range by a transdimensional inversion of Rayleigh-wave travel times. The dispersion data and their uncertainties are inverted for a probabilistic 3-D shear-wave velocity model that includes probability densities for V_s and for the depth of layer interfaces. The probabilistic model is refined by a linearized inversion that accounts for the water layer in the Ligurian Sea. Our *S*-wave velocity and layer boundary probability models correspond well to a recent, high-resolution *P*-wave velocity cross-section derived from controlled-source seismic profiling along the Ligurian-Provence basin axis. A joint interpretation of the *P*- and *S*-wave velocity sections along this profile reveals a thin, anomalous oceanic crust of low *P*-wave velocities but high *S*-wave velocities, intruded by a gabbroic body. The illuminated part of the upper mantle appears to be devoid of serpentinization.

Plain Language Summary The Ligurian-Provence basin (Northwestern Mediterranean Sea) is one of the Miocene-Pliocene back-arc basins that resulted from the retreat of the Adria subduction in the plate reorganization due to Africa-Europe convergence. The crustal structure of the basin is still debated, even though it has been probed by active seismic profiling. We compute a high-resolution shear-wave velocity model of the Ligurian-Provence basin and its margins by making optimal use of ambient-noise recordings of seafloor broadband seismometers. In particular, we improve the usually low quality of surface-wave signals in noise correlations between seafloor stations by involving correlations with land stations. The joint interpretation of our *S*-wave velocity model with a *P*-wave velocity section obtained in the basin axis by controlled-source seismic profiling provides compelling evidence for the presence of a thick sediment pile above a thin, ~4.5 km-thick oceanic crust, intruded by gabbroic bodies emplaced at the crust-mantle transition. These results show the potential of a joint interpretation of *P*- and *S*-wave velocity models since they provide reliable answers to a number of debated questions on the petrological nature of the crust and uppermost mantle, in particular in the Ligurian-Provence basin.

1. Introduction

In the last two decades, the deployment of extensive and dense seismic networks of temporary broadband sensors (e.g., USArray, IberArray) has provided a better understanding of the deep structures of the crust and upper mantle, in particular through the emergence of increasingly more precise 3-D seismic imaging (e.g., Moschetti et al., 2010; Levander et al., 2011). However, many of these dense arrays included exclusively onshore sensors, thus preventing 3-D imaging of continent-ocean transitions and oceanic domains. The AlpArray seismic network (AASN) that covers the European Alps and their foreland, is one of the few dense seismic networks consisting of both onshore and offshore stations (Figure 1; Hetényi et al., 2018). The onshore AASN has been used in ambient-noise imaging studies at the scale of the Alps and Apennines to construct 3-D models of shear-wave velocity (Lu

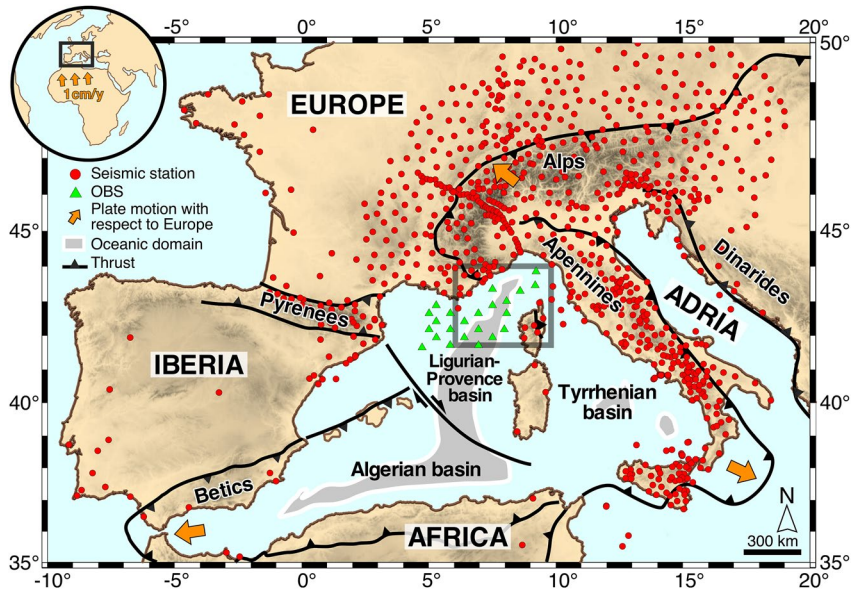

Figure 1. Tectonic map of the western Mediterranean region (modified from Faccenna et al., 2014; Jolivet et al., 2020) with locations of seismic stations used in this work (red circles: onshore sensors; green triangles: AlpArray seismic network ocean-bottom seismometers). The oceanic domains of the Ligurian-Provence, Algerian and Tyrrhenian back-arc basins are filled with gray color. The gray frame shows the location of the map in Figure 8a.

et al., 2018, 2020), attenuation (coda-Q, Soergel et al., 2020), and radial anisotropy (Alder et al., 2021), as well as at the regional scale, for example, Vienna basin (Schippkus et al., 2018), Western Alps (Zhao et al., 2020), Southeastern Alps (Sadeghi-Bagherabadi et al., 2021) and Bohemian Massif (Kvapil et al., 2021). The German-French ocean-bottom seismometers (OBS) of the AlpArray network have been deployed to gain insights into the 3-D structure of the lithosphere beneath the Ligurian-Provence basin and its margins, where major geological/geodynamical issues remain to be clarified. The OBS recordings have been used together with data of onshore permanent and temporary stations in the transdimensional ambient-noise tomography of Nouibat et al. (2022) that covers a large part of Western Europe. In Nouibat et al. (2022), we described the probabilistic inversion strategy for Rayleigh-wave group-velocity maps and their uncertainties, the injection of these uncertainties in the inversion for the V_s model, and the validity of the model in the southwestern Alps. The present paper is a complement to Nouibat et al. (2022) that focuses on the Ligurian-Provence basin. We describe here the specific processing of OBS records and the use of iterative noise correlations that are required to improve ray coverage in the Ligurian Sea, hence improving the model resolution in the basin. We further explain how the water layer and its thickness changes are taken into account in the inversion for *S*-wave velocity. Finally, we compare our V_s model to a V_p section derived from controlled-source seismic profiling along the basin axis.

The geodynamic context of the western Mediterranean region is controlled by the northward motion of Africa (1 cm/yr) with respect to Europe since Late Cretaceous times (Figure 1). This global convergence was accommodated by several collision episodes involving Europe with continental micro-plates (Iberia and Adria), leading to the formation of peri-mediterranean mountain belts (Alps, Apennines, Pyrenees, Dinarides and Betics; e.g., van Hinsbergen et al., 2020). During Miocene and Pliocene times, part of this convergence was accommodated by development of back-arc extensional basins behind the Adria northwest-dipping subduction zone (e.g., Gueguen et al., 1998; Jolivet et al., 2020). This extension started in the Ligurian-Provence basin, and has further spread from west to east, resulting in the opening of the Algerian basin, and later, of the Tyrrhenian basin (e.g., Rollet et al., 2002; Séranne, 1999). Crustal thinning in the central Ligurian basin resulted in the formation of a narrow oceanic domain mainly identified from geophysical data, including seismic reflection, refraction and wide-angle profiling (e.g., Dannowski et al., 2020; Déverchère & Beslier, 1995; Egger et al., 1988), altimetry data and magnetic data from aeromagnetic surveys and reduction to the pole (Sandwell et al., 1995). Although the crust of the central Ligurian basin is considered "atypical" because it is thinner than normal oceanic crust and highlights non-linear magnetic anomalies and a concomitant low gravity anomaly (Bayer et al., 1973; Rollet et al., 2002; Sandwell & Smith, 1997), its petrological and lithological nature is poorly constrained and still debated. Several

hypotheses have been considered: (a) thin oceanic crust with tholeitic volcanism overlying mantle rocks, similar to the Tyrrhenian sea (e.g., Bonatti et al., 1990; Mascle & Rehault, 1990); (b) partly serpentinized peridotites of exhumed upper mantle mostly devoid of volcanic crust (e.g., Beslier et al., 1993; Boillot et al., 1989; Jolivet et al., 2020); (c) thinned and stretched continental crust related to an hyper-extended margin (e.g., Dannowski et al., 2020; McKenzie, 1978; Pascal et al., 1993).

We combine the OBS records of the AlpArray network with those of 890 onshore stations from the AlpArray temporary network, the Cifalps-2 temporary experiment and European permanent networks (Figure 1). Ambient-noise data recorded by OBSs have already been used to build shear-wave velocity and anisotropy models in different regions, for example, South-central Pacific (Harmon et al., 2007), Southeast of Tahiti Island (Takeo et al., 2016) and Western Indian Ocean (Hable et al., 2019). The originality of our approach lies in the specific processing of OBS records and their use within an innovative tomographic framework based on data-driven Bayesian inversions, which has recently been successfully applied to image the lithosphere at the scale of Western Europe (Nouibat et al., 2022). Specific and careful pre-processing of OBS records is compulsory because they are affected by noise sources at the seabed such as compliance and tilting, and they may also be impacted by intrinsic instrumental noise (Crawford & Webb, 2000; Crawford et al., 1998; Deen et al., 2017). Furthermore, OBSs are sensitive to local noise sources such as tides and currents, boat traffic, or marine animals, which are not recorded coherently over long distances (e.g., Batsi et al., 2019). Such noises are therefore unsuitable for ambient-noise tomography, and they even alter the signal-to-noise ratio (SNR) of surface waves reconstructed by noise correlation. Finally, the water column above the seismometers (water depth of 1,100–2,800 m in our case) may have a significant impact on the quality of the Rayleigh-wave dispersion measurements between distant OBSs, particularly at periods shorter than 15 s Wolf et al. (2021) have highlighted the difficulties in using the AASN OBSs to measure Rayleigh waves dispersion curves from noise correlations. These difficulties are partly related to the high level of sea-floor noises. To overcome these difficulties, we propose an innovative way of computing seismic noise correlations using OBS data that consist (a) in a pre-processing of the OBSs noise records that decrease efficiently the seabed noise, and (b) in computing iteratively noise correlations between OBS stations using onshore stations as virtual sources.

The overall methodology and its results are presented in Sections 2–4. Section 2 is dedicated to the description of a specific pre-processing that aims at cleaning OBS daily noise records from instrumental transient glitches and seafloor noises. Section 3 presents how iterative noise correlations are computed between OBSs using onshore stations as virtual sources. In Section 4, we show how noise correlations are used to build a 3-D *S*-wave velocity model of the Ligurian-Provence basin by computing 2-D probabilistic transdimensional Rayleigh wave group velocity maps and their uncertainties at different periods, and by inverting local dispersion curves to derive a probabilistic V_s model. The fifth and final section is dedicated first to a validation of the resulting 3-D V_s model through a comparison with a recent V_p model obtained along a linear refraction, wide-angle seismic profile in the center of the basin by Dannowski et al. (2020). Finally, we show how the combination of the V_p and V_s models along the same profile provides insightful clues to the structure and nature of the crust in the central Ligurian-Provence basin.

2. Data Processing

2.1. Description of the AASN Sea-Bottom Instruments

We processed ambient-noise records from 23 ocean-bottom-seismometers (OBS in Figure 1) that were deployed for eight months in the northwestern Mediterranean Sea as the offshore part of the AlpArray temporary seismic network (AASN; network code Z3). All OBSs were deployed in June 2017 by the AlpArray-OBS cruise of the French R/V "Pourquoi-Pas?" (Crawford, 2017), and recovered in February 2018 by the MSM71 cruise of the German R/V "Maria S. Merian" (Kopp et al., 2018).

Sixteen LOBSTER instruments (Long-term Ocean Bottom Seismometer for Tsunami and Earthquake Research) belong to the GEOMAR and DEPAS pools (German instrument pool for amphibious seismology). Designed by K.U.M. Environmental- and Marine Technology GmbH, these instruments were equipped with HTI-01-PCA hydrophones from High Tech Inc., Trillium compact velocimeters from Nanometrics and K.U.M., and with CMG-40T velocimeters from Güralp for four of them. Seven broadband OBS (BBOBS) belong to the French

OBS pool of INSU-IPGP. Designed by the Scripps Institution of Oceanography, these instruments were equipped with deep-sea differential pressure gauges and Nanometrics Trillium-240 very broadband velocimeters.

The drift of the sensor clocks was measured before the deployment and after the recovery. Recordings were then corrected for clock drift in the RESIF and GEOFON datacenters that archive and distribute the data set. Hable et al. (2018) has demonstrated that the assumption of a linear clock drift is adequate for the ocean-bottom instruments used here.

2.2. Glitch Removal

The first step of the processing of OBS data is the removal of instrumental transient nearly-periodic impulsive noises (glitches) from continuous records of the seven French broadband OBSs (BBOBS in Section 2.1). Indeed, the vertical-component signals exhibit glitches of 1-hr period caused by the activation of the hourly-check of the internal mass centering of the sensor. The pressure component exhibits glitches with a period of 2.65 hr, related to data writing on the hard disk. No glitch was detected on the horizontal components. Similar glitches have been observed in other datasets recorded with the same instruments (e.g., Deen et al., 2017).

Similarly to Deen et al. (2017), we remove glitches from the data using an average glitch waveform matching algorithm. Detailed explanation can be found in Text S1 of the Supporting Information S1. Figure S1 in Supporting Information S1 shows a vertical-component daily record of OBS A416A before and after removing the hourly glitches. It documents the efficiency of the processing by comparing the original signal (in blue), the synthetic glitch signal time series (in red), and the final, glitch-free signal (in black). Similarly, Figure S2 in Supporting Information S1 shows a daily record of the pressure component before and after removing the 2.65-hr-period glitches. The power spectral density curves of an example of 1-day raw and pre-processed vertical component record displayed in Figure 2a, show that removing the glitches reduces the noise level by up to 15 dB at frequencies lower than 10^{-1} Hz.

2.3. Seafloor-Noise Reduction

At frequencies below 5×10^{-2} Hz, the power spectral densities (PSD) of the three-component records of all OBSs are dominated by noise due to compliance and tilt (Figure 2). The compliance is a long-period pressure signal generated by infra-gravity waves induced by pressure variations in the water column (Crawford et al., 1998). Tilting corresponds to displacements and rotations of the sensor induced by seafloor currents that also generate long-period noise. As documented by Figure 2a, long-period noise is stronger on the horizontal components than on the vertical-component. Crawford and Webb (2000) have shown that noise on the vertical-component is lower when the instrument is better leveled. However, long-period noise on the vertical component strongly increases if the instrument is tilted, even slightly, since acceleration induced by seafloor currents on the horizontal components is projected onto the vertical component.

Tilt and compliance noises on the vertical-component records are reduced by using a frequency-dependent response function method (Crawford & Webb, 2000; Crawford et al., 1998). The horizontal components are first corrected for compliance noise by subtracting coherent signals derived from the pressure component. In a second step, tilt noise is reduced in the vertical-component by subtracting coherent signals derived from the compliance-corrected horizontal components (black to green in Figure 2a). Finally, the resulting vertical-component signal is corrected for compliance by subtracting the coherent signal derived from the pressure-component signal (green to purple). Text S2 of the Supporting Information S1 provides a detailed explanation of this procedure.

Figure 2a shows the power spectral density of a daily, vertical-component record of OBS A416A before any correction is applied (blue curve), after correcting from the hourly glitches (black), from the tilt (green) and from the compliance (purple). As shown in Figure 2b, the coherence of the raw vertical-component with the horizontal components (black and blue curves) increases below 5×10^{-2} Hz (see also Figure S3a in Supporting Information S1) while coherence with the pressure component increases around 1.2×10^{-2} Hz. Figure 2a shows that the reduction of the tilt noise (green curve) is maximum (10 dB) at 5×10^{-3} Hz, which is the frequency with the maximum coherence between the vertical component and the two horizontal components. The correction for the compliance noise is almost negligible for this record except around 1.2×10^{-2} Hz, where the coherence between the vertical and the pressure components increases (green area in Figure 2b). Figure S3b in Supporting

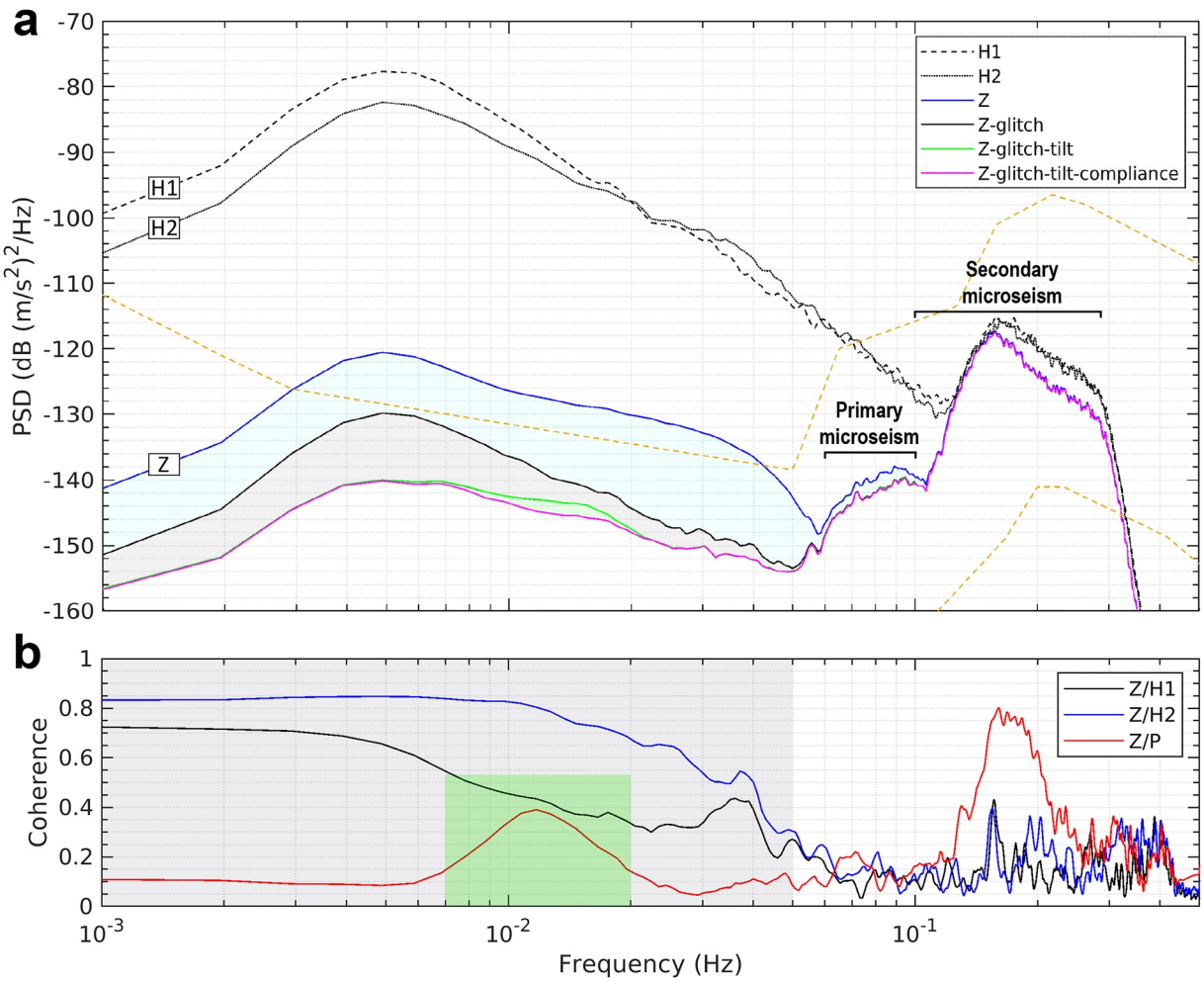

Figure 2. Effect of the different corrections for glitch and seafloor noises on the power spectral densities (PSD) of a 1-day vertical-component record of ocean-bottom seismometer A416A. Raw signals are band-pass filtered between 2.5 and 250 s, corrected from the instrumental response and decimated to 1 Hz sampling frequency. (a) PSDs before and after corrections; Orange dashed lines indicate the Peterson (1993) New Low and High Noise Model (NLNM and NHNM); Blue: PSD of the raw vertical-component record (blue signal in Figure S1a in Supporting Information S1); At frequencies >5×10^{-2} Hz, the PSD is dominated by the primary (~−140 dB) and secondary (~−120 dB) microseisms. At longer periods, the PSD is dominated by the effect of the periodic glitches and the seafloor noises with levels similar to the secondary microseism and higher than the NHNM (in the 3×10^{-3}–4×10^{-2} Hz band) with a peak amplitude at 5×10^{-3} Hz; Black: PSD of the *Z*-component after correction for the 1-hr glitches (black signal in Figure S1a in Supporting Information S1); The −130 dB peak at 5×10^{-3} Hz remains, pointing to its oceanic origin; Its amplitude is weaker than the secondary microseism but still stronger than the primary microseism; Green: PSD of the *Z*-component after correction for the glitches and the tilt noise; Purple: PSD of the *Z*-component after correction for the glitches and seafloor noises; The maximum amplitude of the residual signal is now well below the primary microseism and the NHNM. The dotted and dashed black curves are the PSDs of the horizontal components. Colored areas show the reduction of the noise level after correcting from glitches (blue), from the tilt (gray), and from the compliance (green). (b) Coherence between the vertical channel and the horizontal (blue and black curves) and pressure (red curve) channels. The gray area shows the frequency domain where the *Z*-component is coherent with the horizontal components due to tilt noise. The green area shows the domain where the *Z*-component is coherent with the pressure component due to compliance noise. At frequencies higher than 5×10^{-2} Hz, the coherence is due to primary and secondary microseisms.

Information S1 confirms that the correction for compliance is maximized for this station around 1.2×10^{-2} Hz. In this specific case, the tilt noise is stronger than the compliance noise, which indicates that pressure variations generate less noise than sea-current induced tilt. This strong tilt noise may result from strong currents at the seabed and/or the presence of poorly consolidated sediments directly under the OBS. The lower compliance noise may be due to the large water depth of OBS A416A (~2,630 m), damping the effect of pressure-induced infra-gravity waves.

3. Computation of Noise Correlations and Group-Velocity Measurements

Once OBS records have been corrected for glitches and seafloor noises, we apply the same pre-processing scheme described below to the records of all stations, onshore and offshore, in order to prepare the calculation of inter-station cross-correlations. As explained in Soergel et al. (2020) and Nouibat et al. (2022), we first down-weight the contribution of earthquakes and other high-amplitude transients by removing all 4-hr segments with a peak amplitude four times greater than the standard deviation of the current daily record, and with a RMS greater than 1.5 times the daily mean RMS. Each daily record is then filtered into six period bands (3–5, 5–10, 10–20, 20–40, 40–80 and 80–200 s) and amplitudes are normalized by their envelope. Finally, the 6 filtered and normalized signals are stacked to obtain the 4-hr pre-processed broadband signal.

3.1. First-Order Correlations

As in Nouibat et al. (2022), we compute seismic noise cross-correlations for all station pairs by segments of 4 hr. The 4-hr correlations are normalized and stacked to obtain a single reference correlation per station pair. We use up to 4 years of continuous vertical records for on-land stations pairs, and up to 8 months data to compute correlations for OBS-OBS and OBS-land-station pairs.

As shown by Nouibat et al. (2022) and Figure S4a in Supporting Information S1, Rayleigh waves are clearly visible in the correlations for on-land station pairs in a wide period band (5–150 s). The Rayleigh waves have an average SNR greater than 3.5 (Supplementary Table S1 in Supporting Information S1). Although correlations for OBS-land station pairs are computed from only 8 months of data, Rayleigh waves have a SNR >3 in the 5–70 s period band, except in the 40–70 s band where the SNR is slightly lower (SNR = 2.87, see Figure S4b and Table S1 in Supporting Information S1). These noise correlations can therefore be used for Rayleigh-wave tomography. Figures S4b–S4c in Supporting Information S1 demonstrate the effectiveness of corrections for glitches and seafloor noise in enhancing the SNR of correlations between OBS and land-station records.

First-order correlations between raw OBS records are displayed in the Figure 3a. They can be compared to correlations for land-land station pairs and OBS-land station pairs shown in Figure S4 in Supporting Information S1. The SNR of correlation signals for OBS pairs is poorer than for other types of pairs in all period bands (average SNR <2.6, Table 1). Therefore, Rayleigh waves are hardly detectable at periods shorter than 40 s in OBS-OBS correlations, and undetectable at longer periods (SNR <1.6, Table 1). This may be explained by several factors such as local noises generated around the sensors by seafloor currents, or seismic noises generated between the stations that induce signals around time 0 s of the correlations, masking the Rayleigh waves. Therefore, these first-order OBS-OBS correlations of raw records cannot be used for Rayleigh-wave tomography.

Figure 3b and Table 1 document once again the effectiveness of the corrections for glitches and seafloor noises applied to OBS records, which improve the inter-OBS correlation signals. The correlations have a better SNR and are more symmetrical than those obtained from uncorrected signals, particularly at periods shorter than 40 s (columns a–b of Figure 3). However, correlation signals are still noisy, particularly at short lag times, and accurate measurements of Rayleigh-wave group velocities remain challenging. To further improve the quality of correlations for OBS pairs, we chose to virtually reconstruct the Rayleigh waves by computing iterative correlations.

3.2. Iterative Correlations for OBS-OBS Paths

We have seen in the previous section that correlations for OBS pairs can hardly be used for Rayleigh-wave tomography. Since correlations computed between onshore stations and OBSs exhibit clear Rayleigh waves, we will use onshore stations as virtual sources in order to measure the travel time of Rayleigh waves between OBSs. Indeed, first-order correlations computed between onshore stations and OBSs contain the Rayleigh-wave part of the Green's function. It is thus possible to use them to mimic the case where Rayleigh waves are emitted on the continent and recorded by OBSs. By computing correlations of Rayleigh waves emitted by each virtual source and recorded by two OBSs (i.e., by computing a second-order correlation), it is possible, thanks to the stationary phase theorem, to isolate the Rayleigh-wave propagating between the two OBSs, and therefore to measure its travel time. We explain this with more detail in the following.

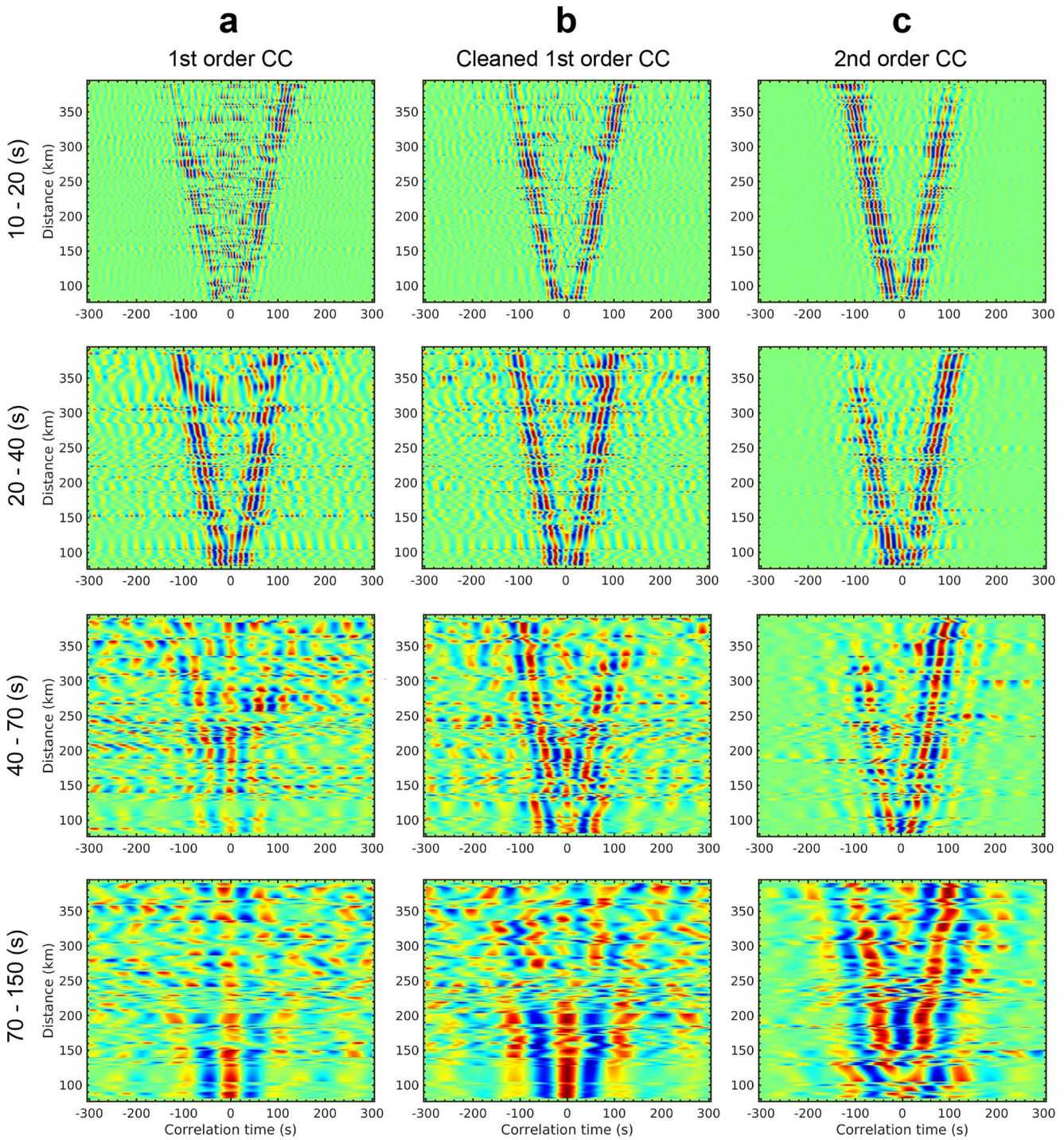

Figure 3. Time-distance plots of correlation signals for ocean-bottom seismometer (OBS)-OBS pairs, obtained in different period bands at different steps of the processing. (a) First-order cross-correlations (C^1s) of raw signals. (b) C^1s of pre-processed signals (glitch removal and seafloor-noise reduction). (c) Second-order correlations (C^2s). The C^1s in (a) are generally of poor quality and poor symmetry, with strong signals at short lag times due to interferences even at short periods. These interferences become stronger with increasing period, and they progressively overshadow the Rayleigh wave-trains. In (b), the C^1 signals are strongly improved due to corrections for glitches and seafloor noises, in particular in the three short- and medium-period bands. The 70–150 s band is still affected by interferences that hide the Rayleigh wave-trains. In (c), the quality and the time-symmetry of correlation signals are significantly improved in all period bands by the calculation of C^2s. In particular, the Rayleigh wave-train emerges from the noise in the long-period band.

Table 1
Signal-to-Noise Ratio and Percentage of Selected Paths for Group-Velocity Tomography in Different Period Bands Using: (a) First-Order Cross-Correlations of Raw Ocean-Bottom Seismometer Vertical-Component Records, (b) First-Order Cross-Correlations of Pre-Processed Signals (Corrected for Glitches, and Seafloor Noises), and (c) Second-Order Cross-Correlations of Pre-Processed Signals

SNR — % of retained paths			
Period band	1st order CC	Cleaned 1st order CC	2nd order CC
10–20 s	2.52%–2.45%	3.29%–8.11%	5.77%–39.6%
20–40 s	2.32%–1.52%	3.61%–11.5%	5.62%–23.4%
40–70 s	1.57%–0.03%	3.12%–5.22%	4.52%–14.3%
70–150 s	1.13%–0.01%	1.42%–2.61%	4.37%–7.31%

Let us consider any medium with a distribution of sources f. The wavefield recorded at a station A can be expressed using the Green's function G of the medium:

$$u\left(\vec{r}_A,t\right) = \int_\Omega \int_0^\infty G\left(\vec{r}_s,\vec{r}_A,t'\right)\ f\left(\vec{r}_s,t-t'\right)\ dt'\ d\vec{r}_s \tag{1}$$

It has been shown that the time-derivative of the first-order cross-correlation $C^1_{\vec{r}_A,\vec{r}_B}(\tau)$ computed between wavefields recorded at two stations A and B is the Green's function $G_{\vec{r}_A,\vec{r}_B}(t)$ of the medium, assuming for instance a perfectly homogeneous distribution of white noise everywhere in the medium (e.g., de Verdière, 2006; Lobkis & Weaver, 2001; Roux et al., 2005; Snieder, 2004; Wapenaar, 2004; Weaver, 2005):

$$\frac{d}{d\tau}C^1_{\vec{r}_A,\vec{r}_B}(\tau) = G_{\vec{r}_A,\vec{r}_B}(\tau) \tag{2}$$

In the case where all white noise sources are spatially uncorrelated, the correlation of wavefields recorded at A and B can be rewritten as the integral of correlations between $G\left(\vec{r},\vec{r}_A\right)$ and $G\left(\vec{r},\vec{r}_B\right)$:

$$\begin{aligned} C^1\left(\vec{r}_A,\vec{r}_B,\tau\right) &= \int_0^\infty u\left(\vec{r}_A,t\right)\ u\left(\vec{r}_B,t+\tau\right)\ dt \\ &= \int_\Omega \int_0^\infty G\left(\vec{r}_s,\vec{r}_A,t'\right)\ f\left(\vec{r}_s,t-t'\right)\ dt'\ d\vec{r}_s \otimes \int_\Omega \int_0^\infty G\left(\vec{r}_s,\vec{r}_B,t'\right)\ f\left(\vec{r}_s,t-t'\right)\ dt'\ d\vec{r}_s \\ &= \int_\Omega\ G\left(\vec{r}_s,\vec{r}_A,t\right) \otimes G\left(\vec{r}_s,\vec{r}_B,t\right)\ d\vec{r}_s \end{aligned} \tag{3}$$

where $\otimes$ denotes the cross-correlation operation. Since the time-derivative of correlations is similar to the Green's function of the medium, it follows immediately by substituting dC^1/dt to G in Equation 3 that the first-order correlation is equivalent to a second-order correlation that we will note C^2:

$$C^1\left(\vec{r}_A,\vec{r}_B,\tau\right) = \int_\Omega\ \frac{d}{dt}C^1\left(\vec{r}_s,\vec{r}_A,t\right) \otimes \frac{d}{dt}C^1\left(\vec{r}_s,\vec{r}_B,t\right)\ d\vec{r}_s = C^2\left(\vec{r}_A,\vec{r}_B,\tau\right) \tag{4}$$

Equation 4 indicates that it is possible to reconstruct the Green's function of the medium between A and B by re-correlating the noise correlations computed between each point of the medium and stations A and B. However, this demonstration assumes that the time-derivative of correlations are the exact and complete Green's function of the medium. The assumption would be correct if stations that could be used as virtual sources would exist everywhere in the medium.

In practice, the seismic noise recorded at the Earth surface in the period band considered in this work (5–150 s) is dominated by Rayleigh waves. As a consequence, noise correlations computed between onshore stations and OBSs do not provide the full Green's function of the medium including all propagating modes, but they do provide robust estimates of the travel time of Rayleigh waves.

Rather than attempting to reconstruct the full Green's function, we will measure the travel time of the Rayleigh waves between OBSs A and B by using a simplified approach inspired by Equation 4. It consists in re-correlating only the Rayleigh-wave parts of the correlations computed between onshore stations and OBSs A and B, that we consider as the Rayleigh-wave part of the Green's function:

$$\begin{aligned} \frac{d}{d\tau}C^{2,Ray}\left(\vec{r}_A,\vec{r}_B,\tau\right) &= \frac{d}{d\tau}\int_\Omega\ \frac{d}{dt}C^{1,Ray}\left(\vec{r}_s,\vec{r}_A,t\right) \otimes \frac{d}{dt}C^{1,Ray}\left(\vec{r}_s,\vec{r}_B,t\right)\ d\vec{r}_s \\ &\approx G^{Ray}\left(\vec{r}_A,\vec{r}_B,\tau\right) \end{aligned} \tag{5}$$

where superscript "Ray" indicates that we only correlate the fundamental mode of Rayleigh waves of first-order correlations. In that way, we only retrieve the fundamental mode of the Rayleigh-wave part of the Green's function.

In practice, the distribution of virtual sources is never homogeneous. Instead, we use land stations deployed all over Western Europe, while OBSs are located in the Ligurian Sea (Figure 1). Therefore, the condition of the stationary phase theorem are not completely met. To circumvent this difficulty, we select virtual sources that

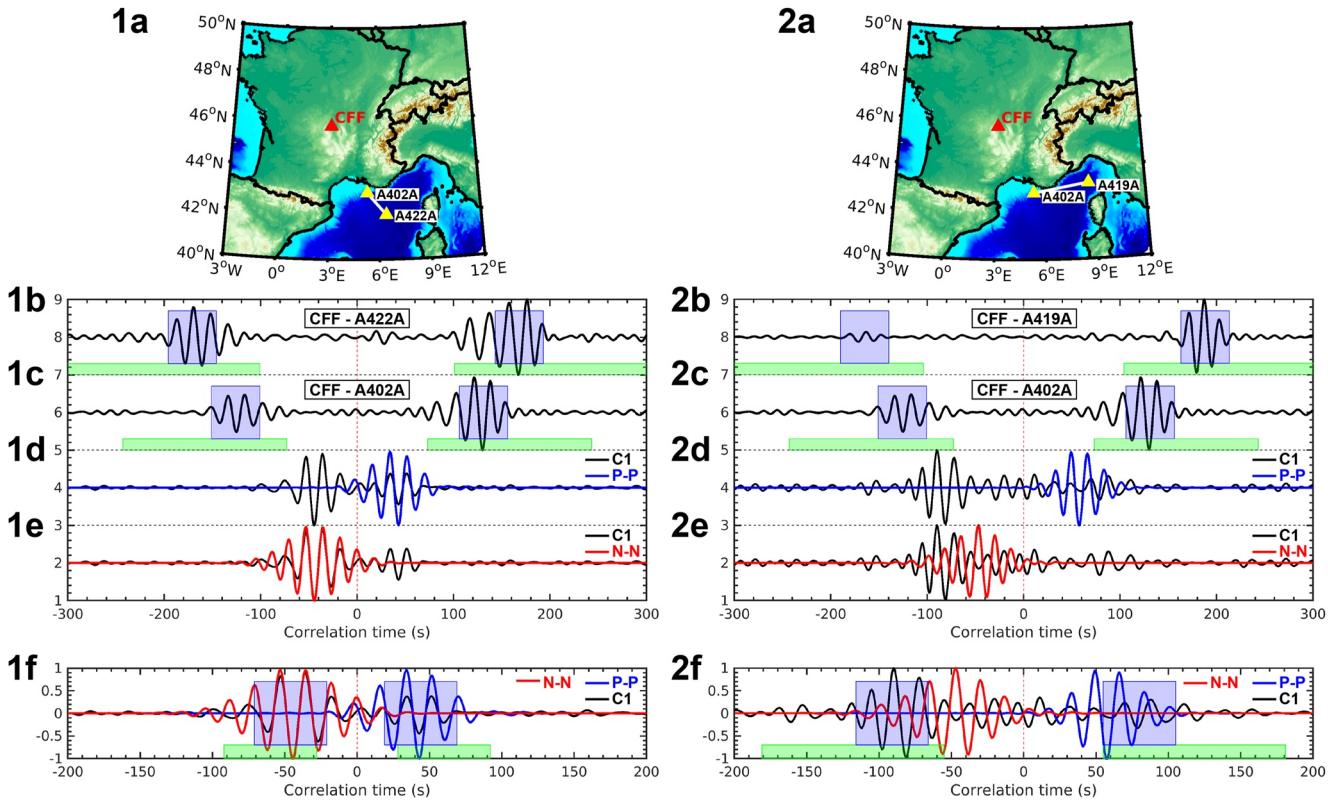

Figure 4. Details of the computation of second-order correlations for two examples of ocean-bottom seismometer (OBS)-OBS pairs, using station CFF (FR network) as virtual source. (1–2a): Station location maps. In example (1), the virtual source is roughly aligned with the OBS pair, while in example (2), the azimuth of the virtual source is almost perpendicular to the pair. (1–2b, 1–2c): First-order correlation signals between CFF and each OBS. The green areas show the Rayleigh-wave search windows (wave propagation of 1–5 km/s over the inter-station distances). The blue areas show the Rayleigh-wave detection windows. (1–2d): First-order correlation of the OBS signals (C^1, in black), and correlation of the positive-time (causal) parts of the C^1s between CFF and the OBS couple (P-P, in blue). (1–2e) First-order correlation of the OBS signals (C^1, black), and correlation of the negative-time (acausal) parts of the C^1s between CFF and the OBS couple (N-N, red). (1–2f): Comparison of the causal (P-P, blue) and acausal (N-N, red) C^2s (that will be summed to obtain the final C^2), with the first-order correlation of the OBS signals (C^1, black). The C^2 and C^1 signals have similar phases in (1) where the virtual source is aligned with the OBS pair. They have incoherent phases in (2), since CFF is not located in the end-fire lobe of this OBS pair (see text).

are expected to contribute constructively to the correlations (Figure 4). To that end, we design a virtual-source azimuthal-filter that only retains sources located in the end-fire lobe of the OBS couple, that is in azimuths at ±20° with respect to the azimuth of the OBS pair. Moreover, we enhance the virtual source coverage by using separately the causal and anticausal parts of the first-order correlations to compute the second-order correlation.

Because onshore stations are well distributed and OBS-onshore correlations exhibit clear Rayleigh waves, the use of virtual sources in iterative correlations for OBS-OBS paths leads to a higher quality of Rayleigh waveforms (columns b–c of Figure 3 and Table 1). This is achieved through: (a) separately recovering the causal and anticausal parts of the Green's function by using separately the causal and anticausal parts of the first-order correlations, thus avoiding interferences at long periods, and (b) controlling the distribution of virtual sources, thus guaranteeing a higher quality of the C^2s by contrast to OBS-OBS C^1s that exhibit low SNR probably due to local noise sources. These local noise sources do not contribute significantly to OBS-onshore stations paths, and therefore neither to second-order correlations. Figure S5 in Supporting Information S1 shows that phases of the Rayleigh waveforms reconstructed from the C^1 and C^2 processes match. In the 5–10 s band, iterative correlations do not systematically improve the signal quality as compared to first-order correlations. Therefore, we select for each path the correlation of highest quality after checking that the C^1 and C^2 are coherent.

The strengths of the iterative correlations make it possible to substantially improve the path coverage in the Ligurian-Provence domain (Table 1). Our results demonstrate the efficiency of this method in providing robust group-velocity measurements. Further illustration and validation will be the subject of a future paper.

3.3. Group-Velocity Measurements

Once first-order and iterative correlations have been computed for onshore and offshore stations respectively, we derive group-velocity dispersion curves of the causal and acausal parts of the correlations by using multiple filter analysis (MFA, Dziewonski et al., 1969; Herrmann, 1973). As in Nouibat et al. (2022), we adapt the width of the Gaussian filter to the inter-station distance to accommodate the trade-off in resolution between the time and frequency domains (Levshin et al., 1989). We correct our group-velocity measurements from the biases that occur when the MFA method is applied on signals having a non-flat spectrum (Shapiro & Singh, 1999). This is especially important when measuring Rayleigh-wave velocities using noise correlations around the first and second microseismic peak, that is, around 7 and 14 s.

In order to build the group-velocity maps in the Ligurian-Provence domain, we maximize the path coverage over the Ligurian Sea by using simultaneously OBS-OBS, land-land, and land-OBS station pairs. A careful selection of group-velocity measurements is achieved to keep the most reliable ones and discard those that are biased by an unfavorable distribution of noise sources, or by interferences of causal and acausal Rayleigh waves for instance.

For first-order correlations (C^1s) computed between land-land and land-OBS stations, at each period, we keep measurements if: (a) the SNR defined as the ratio of the Raleigh-wave peak amplitude and the standard deviation of the following signal, is greater than three on the positive and negative correlation times, (b) group velocities measured in positive and negative correlation times differ by less than 0.2 km/s, and (c) the inter-station distance is greater than 2 wavelengths. For iterative correlations (C^2s) computed between OBS stations, we do not use the SNR criteria, since iterative correlations only exhibit the fundamental mode of the Rayleigh waves, owing to their construction. Nevertheless, for each C^2 satisfying the distance and symmetry criteria, we only keep the group-velocity measurement of the side of the correlation (positive or negative time) where the amplitude of the Rayleigh-wave is maximum (i.e., where we have more virtual sources contributing).

Table 1 shows that for OBS-OBS pairs, the selection procedure would reject more than 97% of Rayleigh waves velocity measurements performed on first-order correlations computed using OBS data that were not corrected from the compliance and tilt noises. This illustrates that these signals are obviously not useable for ambient-noise tomography. By contrast, we selected between 2.6% and 11.5% of the measurements performed on first-order correlations done using OBS data corrected from sea floor noises. This highlights the importance of the pre-processing scheme described in Section 2. Moreover, we kept between 7.3% and 39.6% of group-velocity measurements performed on iterative correlations (C^2s) depending on the period-band considered. Second-order correlations provide a substantial gain over first-order correlations, leading to a significant improvement of the raypath coverage in the Ligurian-Provence basin with respect to the ANT of Wolf et al. (2021) based on first-order correlations.

4. 3-D Shear-Wave Velocity Model

4.1. Inversion for 2-D Group-Velocity Maps

We compute 2-D group-velocity maps and associated uncertainties using a "data-driven" transdimensional approach at discrete periods from 4 to 150 s. At each period, probabilistic group-velocity maps are derived by exploring millions of 2-D models using the reversible-jump Markov-chain Monte-Carlo method (rj-McMC, Bodin et al., 2012). The method used for the inversion and the spatial resolution of the resulting group-velocity maps are discussed in detail in Nouibat et al. (2022). Uncertainty and path density maps at different periods are presented in Figure S6 in Supporting Information S1.

Resulting group-velocity maps of the Ligurian-Provence basin and its margins are shown in Figure 5 for periods from 6 to 35 s. The 6 and 8 s maps (sensitive to ∼4–8 km depth) highlight low-velocity anomalies ($U < 1.6$ km/s) in the central and southwestern parts of the basin (C-SLPB in Figure 5), that are probably associated with thick sediment sequences. These velocities are lower than those of the southeast-France basin and the Gulf of Lion (respectively SFB and GL in Figure 5). The northeastern Ligurian-Provence basin (NLPB), its northern, Provence coast margin and its southern margin in Corsica have larger velocities ($U \geq 2.4$ km/s). From simulations of Rayleigh-wave dispersion in synthetic 1-D models, we show that such periods are also highly sensitive to the presence and thickness of the water column (Figure S7 in Supporting Information S1). The 10 s map still shows velocities lower than 2.5 km/s in the central and southwestern Ligurian-Provence basin. The 12 and 15 s maps

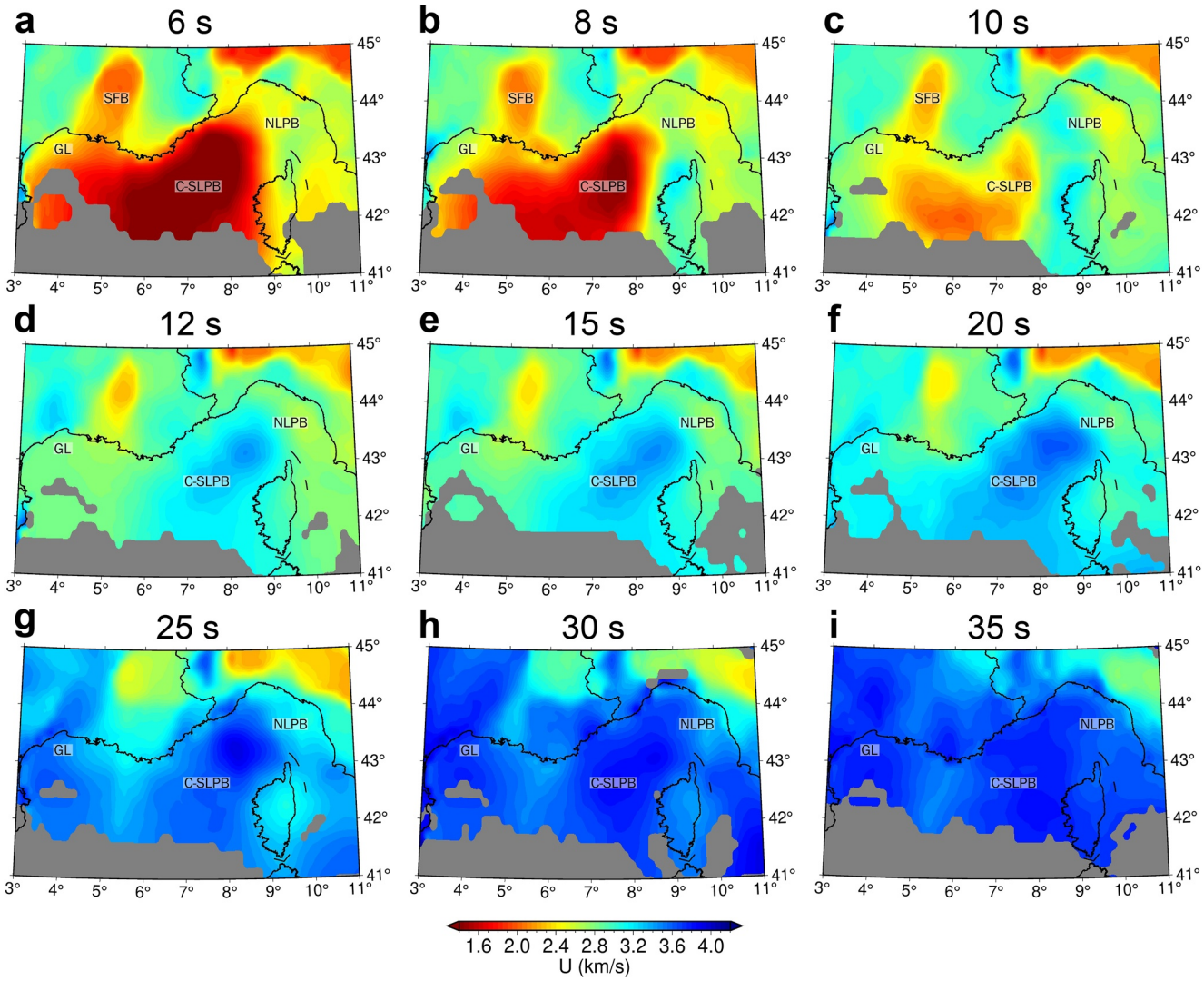

Figure 5. Group-velocity maps (average solutions) at 6–35 s periods, obtained with the Hierarchical Bayes reversible-jump algorithm. Only areas with uncertainty lower than 0.5 km/s are shown. C-SLPB: central and southwestern parts of the basin, GL: Gulf of Lion, NLPB: northeastern Ligurian-Provence basin, SFB: southeast-France basin.

(sensitive to ∼10–15 km depths) highlight velocities larger than 3.5 km/s associated with the thin crust of the Ligurian basin. However, the northeastern basin has lower velocities indicative of a deeper Moho in the Gulf of Genova. Velocities lower than 3.2 km/s correspond to thick crust under Corsica and the Provence coast. At 25 s period (sensitive to ∼15–30 km depth), velocities are still lower along the western coast of the Gulf of Genova than in the basin, indicative of a thicker crust, as in Corsica. At 30 s and 35 s periods, group velocities are homogeneous and exhibit large velocities ($U > 3.5$ km/s) in most of the study region.

4.2. Inversion for Shear-Wave Velocity

The group-velocity maps and their uncertainties are used to derive a 3-D V_s model. For this, we perform a two-step data-driven inversion to tackle the non-unicity of the inverse problem. The main part of this process is described in detail in Nouibat et al. (2022), so we will only summarize it here. We will rather focus on the specificity of the inversion for the offshore region, which is the consideration of the water layer. A result of the inversion for V_s at an offshore location in the Ligurian Sea is shown in Figure S8 in Supporting Information S1.

First, a 3-D probabilistic solution is computed that gives at each location the probability distribution of V_s and the probability of having an interface as a function of depth. This is achieved using an exhaustive grid search on a set of ∼130 million synthetic four-layer models, which include a sedimentary layer, the upper crust, the lower crust and a half-space representing the upper mantle. The strength of this first-step Bayesian framework lies in constraining the structural complexity of the crust (i.e., of the short-period part of the dispersion curve) by means of an ensemble of models, fitting the dispersion curve to the degree required by its uncertainties. However, due to the four-layer model assumption, this procedure is not sufficient to fully describe the complexity of the model structure, particularly in the mantle part, that is in the long-period part of the dispersion curve. Hence, we use an iterative linear least-square inversion (Herrmann, 2013) as a complement to update the mantle part of the model and further refine the fit to the local dispersion curve for the crustal part (Figure S8 in Supporting Information S1).

The initial model for the linear inversion (second step) at a given location is the average of all selected probabilistic solutions of the first inversion step, weighted by their likelihood values. We discretize the crustal and mantle parts at intervals of 1 and 5 km, respectively, and assume a gradual increase of V_s below Moho according to the global model PREM (Dziewonski & Anderson, 1981). For offshore locations, we incorporate on top of this initial model an additional layer of thickness equal to water depth at the given location. The parameters of this water layer are kept fixed during the linear least-square inversion (thickness, $V_s = 0$ km/s, $V_p = 1.5$ km/s, $\rho = 1 \times 10^3$ kg/m^3). Since we invert for short periods as well, an appropriate parameterization of the water column is crucial. Indeed, we highlight its influence by computing group-velocity dispersion curves for synthetic four-layer crustal models representative of the oceanic crust of the Ligurian-Provence basin, and different water levels from 0 to 3.1 km (Figure S7 in Supporting Information S1). This shows that the effect of the water layer on the dispersion curve is substantial at periods shorter than 15–20 s, where the water depth changes impact: (a) the absolute group velocities, and (b) the shape of the dispersion curve, particularly in the vicinity of the Airy phase.

Figure 6 shows depth slices in the 3-D shear-wave velocity model at 3–30 km depth. The sediment layer is clearly visible at 3–7 km depth in the central and southwestern Ligurian-Provence basin, with low velocities of 2–3.2 km/s. The transition from crustal (3.5–4.1 km/s) to mantle velocities (4.1–4.5 km/s) is located between 10 km and 12–15 km in the parts of the basin with thinnest crust. Between 20 and 30 km, areas of strong velocities corresponding to the mantle extend westward from the Ligurian-Provence basin to the Gulf of Lion across a nearly N–S transition of slower velocities at ∼5.5°E.

4.3. Comparison With the V_s Model by Wolf et al. (2021)

Figure 7 shows a comparison of our V_s model and the model by Wolf et al. (2021), which was the first published ambient-noise tomography using data of AlpArray OBSs in the Ligurian basin. Our V_s model covers a wider area as part of the large-scale model by Nouibat et al. (2022) that uses all available broadband stations in Western Europe.

At 3-km depth, our model (Figure 71a) highlights: (a) the sedimentary cover in the central and southwestern basin (1.8–2.2 km/s), where Wolf et al.'s model (Figure 71b) exhibits patches of very low velocities ($V_s \leq 1.4$ km/s), and (b) gradual increasing of velocity from the central basin toward the conjugate margins, which is not clearly visible in Wolf et al.'s model where velocities fluctuate from very low ($V_s \leq 1.8$ km/s) to high values (2.4–2.5 km/s). At 5-km depth, we still observe typical sediment velocities (Figure 72a), while Wolf et al.'s model (Figure 72b) exhibits higher velocities ($V_s > 3.5$ km/s). At 13-km depth, our model (Figure 73a) shows almost homogeneous mantle velocities in the basin ($V_s \geq 4.1$ km/s) while Wolf et al.'s model (Figure 73b) exhibits numerous small-size velocity anomalies, fluctuating between mantle-like ($V_s \geq 4.1$ km/s) and crust-like velocities ($V_s \leq 3.7$ km/s). These heterogeneities suggest a much more irregular Moho surface than in our model. At 20-km depth, our model (Figure 74a) documents crustal thinning toward the basin axis with V_s increasing across the conjugate margins. Again, velocities in the central basin are more heterogeneous in Wolf et al.'s model (Figure 74b), with localized small-size anomalies. Although the transition domain has an irregular shape in Wolf et al.'s model, it remains to first order similar to that shown in our model.

We think that such strong differences between the two V_s models are mostly due to differences in coverage and quality of Rayleigh-wave dispersion data. Indeed, we greatly enhanced the path coverage in the Ligurian basin by using iterative correlations for OBS-OBS paths. In addition, the use of all broadband stations in Western Europe

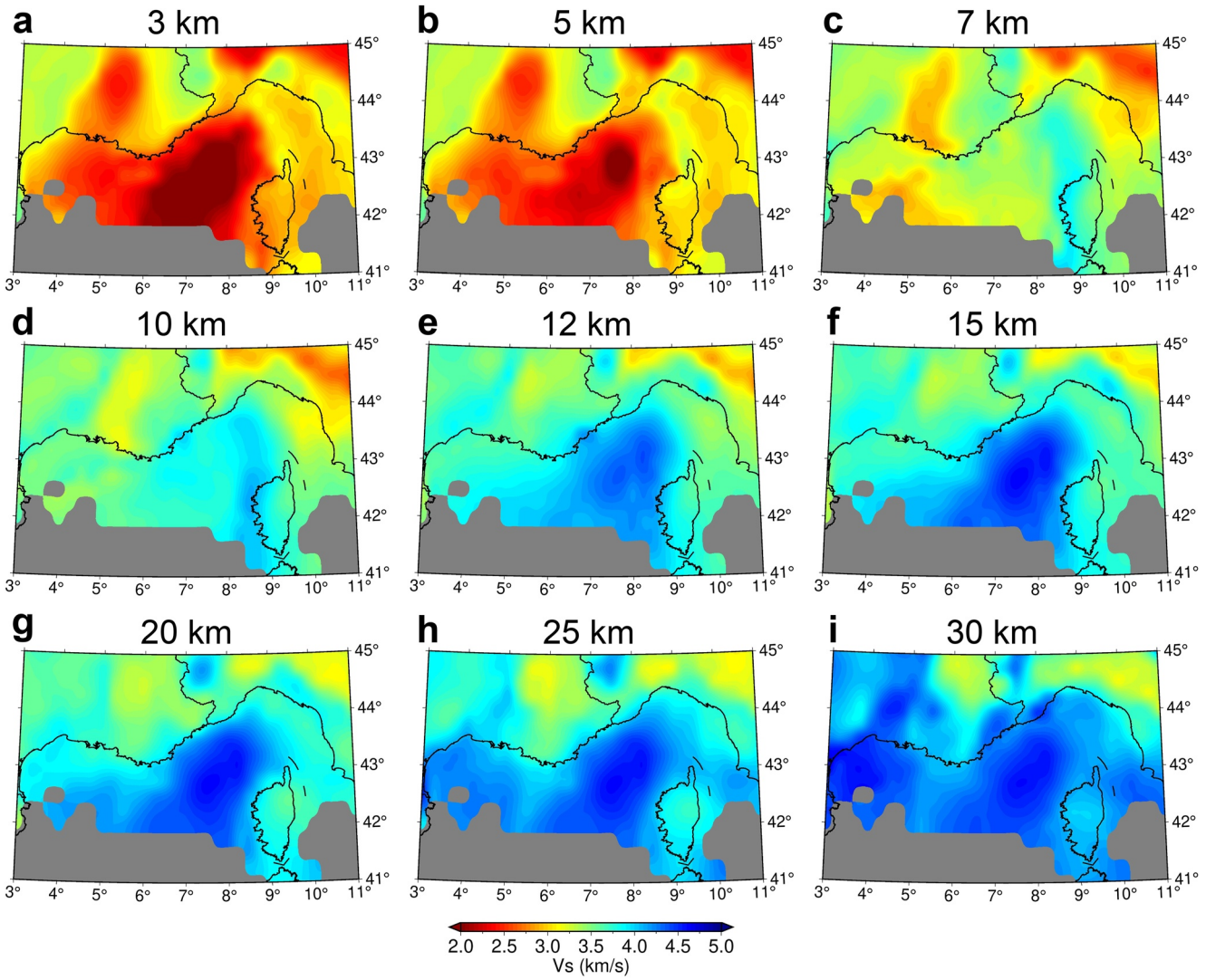

Figure 6. Depth slices in the final V_s model at 3–30 km depths. Only regions with 1σ error <8% are shown.

provides long ray paths across the Ligurian Sea, allowing us to improve path coverage to the west and southeast and make use of Rayleigh-wave dispersion measurements up to 150 s. On the other hand, Wolf et al. (2021) used only 23 onshore stations nearby the basin, thus a limited aperture. Therefore, they used earthquake records for periods greater than 20 s. To a lesser extent, the differences between the two models may also be explained by the different strategies used to invert Rayleigh-wave dispersion measurements. Wolf et al. (2021) computed their 2-D dispersion maps using a linear inversion that depends on an explicit regularization, while our transdimensional approach does not. Moreover, our 1-D Bayesian inversion for V_s take uncertainties on dispersion measurements into account, which is key for controlling model complexity.

As we will see in the following section, our V_s model is more coherent with current knowledge on the crustal structure of the Ligurian-Provence basin than the one by Wolf et al. (2021). In particular, the thickness of the sedimentary cover and Moho depth and geometry estimated from our V_s model are coherent with the V_p model by Dannowski et al. (2020) along the basin axis and with the stratigraphic log after Leprêtre et al. (2013).

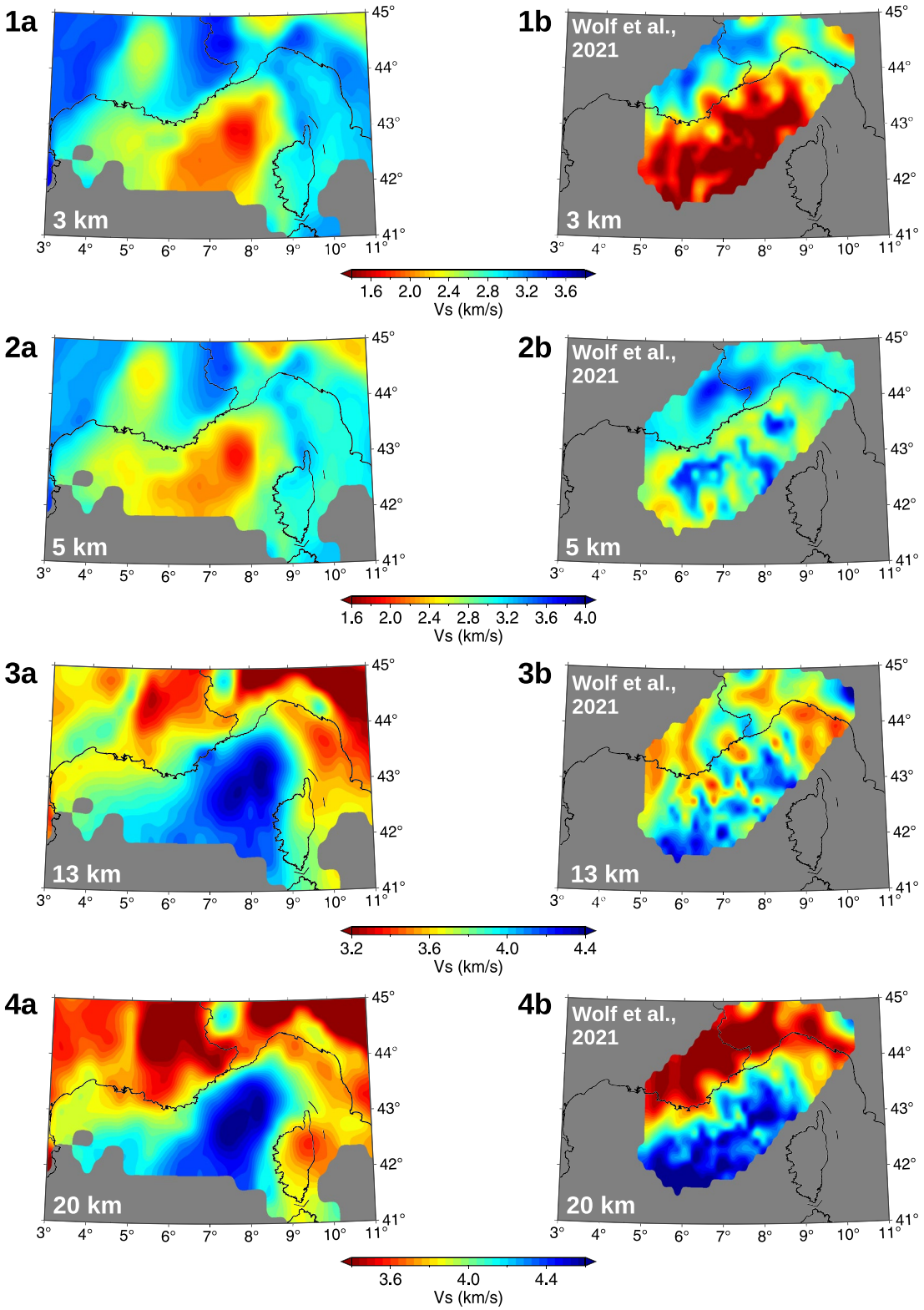

Figure 7. Comparison between our V_s model (left panel) and the V_s model by Wolf et al. (2021) (right panel) at four depths.

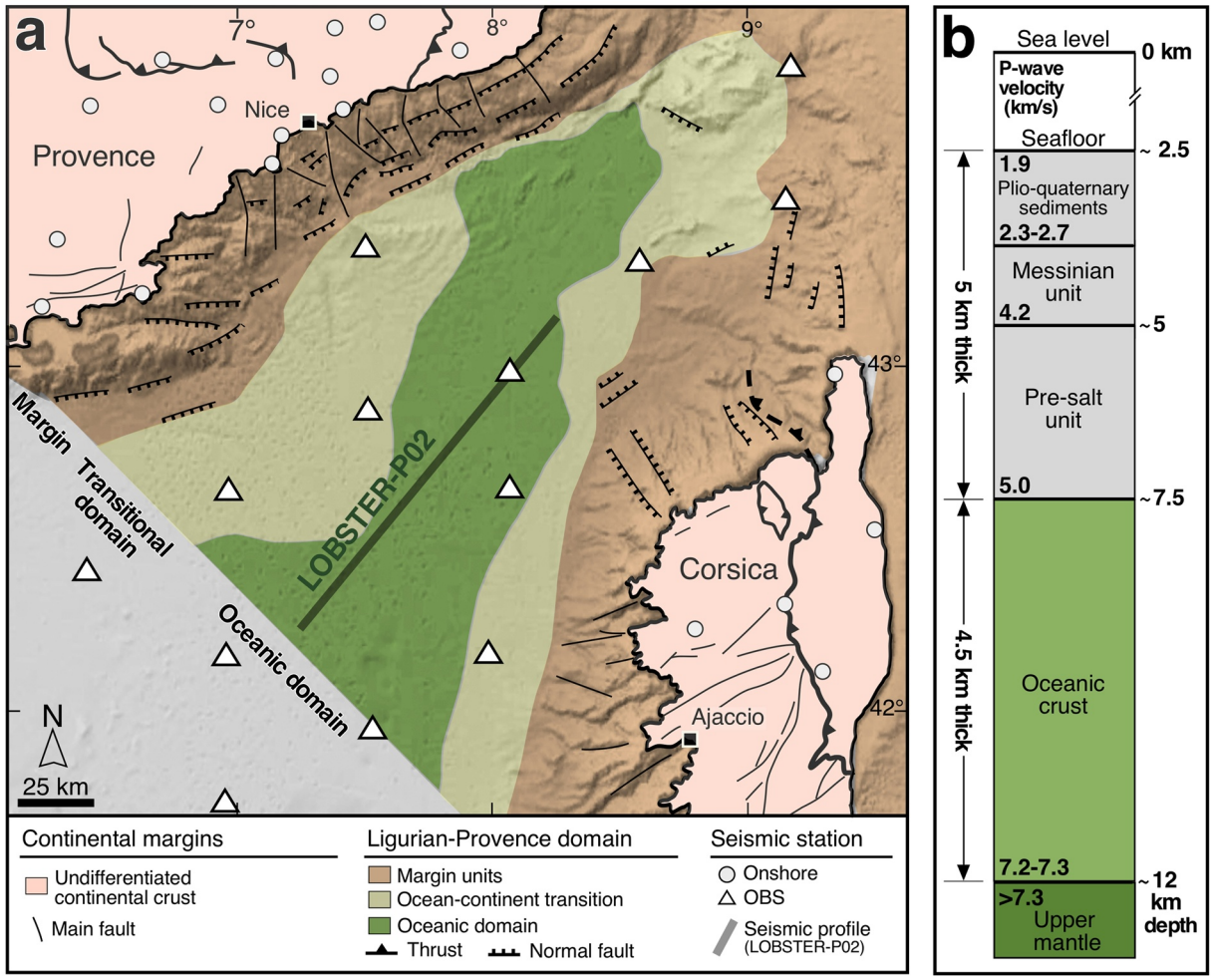

Figure 8. (a) Geological and tectonic setting of the Ligurian-Provence basin and European domains of southeast France and Corsica, showing: (1) continental margins, (2) transitional domains, and (3) the central oceanic domain. Gray line: trace of the seismic profile used in the discussion (Dannowski et al., 2020). Seismic stations are indicated by white triangles (AASN OBSs) and white circles (onshore stations). (b) stratigraphic log showing *P*-wave velocity and thickness of geological units observed in Western Mediterranean oceanic basins (after Leprêtre et al., 2013).

5. Discussion

We now focus on the oceanic domain of the Ligurian-Provence basin (Figure 8a), in particular on the comparison of our *S*-wave velocity model with a recent *P*-wave velocity model derived by Dannowski et al. (2020) from a controlled-source seismic profile recorded along the basin axis (thick black line in Figure 8a). The availability of this high-resolution V_p section provides a unique opportunity to assess the accuracy and validate our V_s model against an independent data set. Moreover, the existence of V_p and V_s models along the same profile may provide clues on the petrological structure of the crust in the oceanic domain of the basin, which is still debated. Indeed, it has been proposed that the oceanic domain is made of an oceanic crust with a thin basaltic layer (e.g., Bonatti et al., 1990; Mascle & Rehault, 1990), or an exhumed and serpentinized mantle devoid of any volcanic upper layer (e.g., Beslier et al., 1993; Boillot et al., 1989; Jolivet et al., 2020), or even an hyper-extended continental crust (e.g., Dannowski et al., 2020; McKenzie, 1978; Pascal et al., 1993).

5.1. Geological Setting of the Ligurian-Provence Basin

The basin opening initiated at 30 Ma by a rifting phase between Europe and the Corsica-Sardinia block, as a result of back-arc extension above the Adria oceanic micro-plate, initially subducting north-westward (e.g., Faccenna et al., 1997). The progressive south-eastward roll-back and retreat of the Adria slab below the Corsica-Sardinia

domain led to stretching of the continental crust followed by continental break-up during the early Miocene, and to the genesis of an oceanic crust between 20 and 15 Ma (Séranne, 1999). As a result, the Ligurian-Provence basin includes two thinned conjugate continental passive margins separated by an oceanic domain (Figure 8a). According to Rollet et al. (2002), the entire region is characterized by magnetic anomalies, and by the presence of magmatic bodies identified from acoustic facies in seismic reflection profiles. The area between the margins and the oceanic domain is described as a transitional domain, likely made up of a very thin continental crust overlying a thick rift-related corner of magmatic underplating (e.g., Séranne, 1999). This limit is marked by an abrupt change in the amplitude of magnetic anomalies with a transition from mostly positive values in the deep basin (i.e., oceanic domain) to negative values at the continent-ocean transition, and by a change in acoustic facies on seismic reflection profiles (e.g., Déverchère & Beslier, 1995; Réhault et al., 1984; Rollet et al., 2002). While the magmatism occurring in the margins has been associated to back-arc magmatic activity strongly influenced by subduction (e.g., Bellon, 1981; Coulon, 1977; Réhault et al., 2012), the nature of magmatism observed in the oceanic domain remains unknown. It could not be investigated by direct geochemical analysis due to the presence of a sedimentary cover several kilometers thick.

Figure 8b shows a stratigraphic log representative of Western Mediterranean oceanic basins that includes *P*-wave velocity estimates. It is derived from the results of joint seismic wide-angle and reflection profiling in the Algerian and Western Sardinia basins (Gailler et al., 2009; Klingelhoefer et al., 2008; Leprêtre et al., 2013). The sedimentary layer of 5-km average thickness and 1.9–5 km/s *P*-wave velocities is made up of Plio-quaternary sediments, Messinian and pre-salt units (Figure 8b). The transition from Plio-quaternary to Messinian units occurs at $V_p \approx 2.5$ km/s. The Messinian sequence exhibits strong thickness variations ascribed to salt diapirism. It is separated from the pre-salt unit by the 4.2 km/s velocity boundary. The deepest sediments overlay an oceanic basement that starts at $V_p > 5$ km/s. The oceanic crust is relatively thin with an average thickness of 4.5 km. Its *P*-wave velocities range from 5 to 7.2–7.3 km/s at ∼12 km depth, which corresponds to the Moho depth ($V_p > 7.3$ km/s in the upper mantle). Controlled-source seismic data are useful to constrain the layer thicknesses and the depths of major interfaces (intra-sedimentary, sediment-crust and Moho), but their interpretation in terms of petrology only rely on *P*-wave velocity estimates. The interpretation is ambiguous as two lithologies of different petrological natures may have similar V_p (or V_s) signatures. However, *P*- and *S*-wave velocities can be used jointly to yield information on lithologies and their hydration degree (e.g., Grevemeyer et al., 2018; Malusà et al., 2021). For instance, the V_p/V_s ratio is commonly used to assess the degree of serpentinization in oceanic domains and margins (e.g., Bullock & Minshull, 2005; Grevemeyer et al., 2018; Reynard, 2013). We will take advantage of the availability of the V_p cross-section by Dannowski et al. (2020) and our V_s section along the same profile to further constrain the petrological nature of the crust in the central Ligurian-Provence basin.

5.2. Seismic Velocity Cross-Sections in the Central Oceanic Domain

Figures 9a and 9b show vertical sections through our 3-D V_s model and probability of presence of interfaces along the SW-NE transect investigated by Dannowski et al. (2020). The *P*-wave velocity section of Dannowski et al. (2020) is shown in Figure 9c.

Figure 9b shows two major layer boundaries at ∼5 and ∼12 km depth with rather high probabilities of presence, and a third one of weaker probability at ∼7.5 km depth. The good correspondence of the shallowest boundary with the velocity contour $V_s = 2.5$ km/s suggests that it is probably an intra-sedimentary interface. This boundary also coincides with the 4.2 km/s *P*-wave velocity contour (Figure 9c), which corresponds to the base of the Messinian salt unit according to Figure 8b. This interpretation is consistent with *S*- and *P*-wave velocities, typical of salt (e.g., Yan et al., 2016). The intermediate interface at ∼7.5 km depth, which is slightly less pronounced that the Moho boundary (Figure 9b) coincides with the velocity contours $V_s = 3.5$ km/s (Figure 9b) and $V_p = 5$ km/s (Figure 9c), which may support its interpretation as the sediment-crust boundary, in agreement with Figure 8b. However, this interface does not correspond to a marked change in seismic velocity in the final model of Figure 9a. Therefore, we cannot detect unambiguously the depth of the sediment-crust transition. We will use the proxy $V_s = 3.5$ km/s (or $V_p = 5$ km/s) for the sediment-crust boundary.

In the northeastern part of the transect ($x > 70$ km), the lower crust has higher, but still crustal *P*-wave velocities (6.0–7.2 km/s, in green in Figure 9c), hence a weaker *P*-wave velocity gradient at the Moho than in the southwestern part. By contrast, *S*-wave velocities are high and almost mantle-like (4.0–4.4 km/s), with a low *S*-wave velocity gradient at Moho depth, in particular at the northeastern end of the profile ($x > 90$ km in Figure 9a).

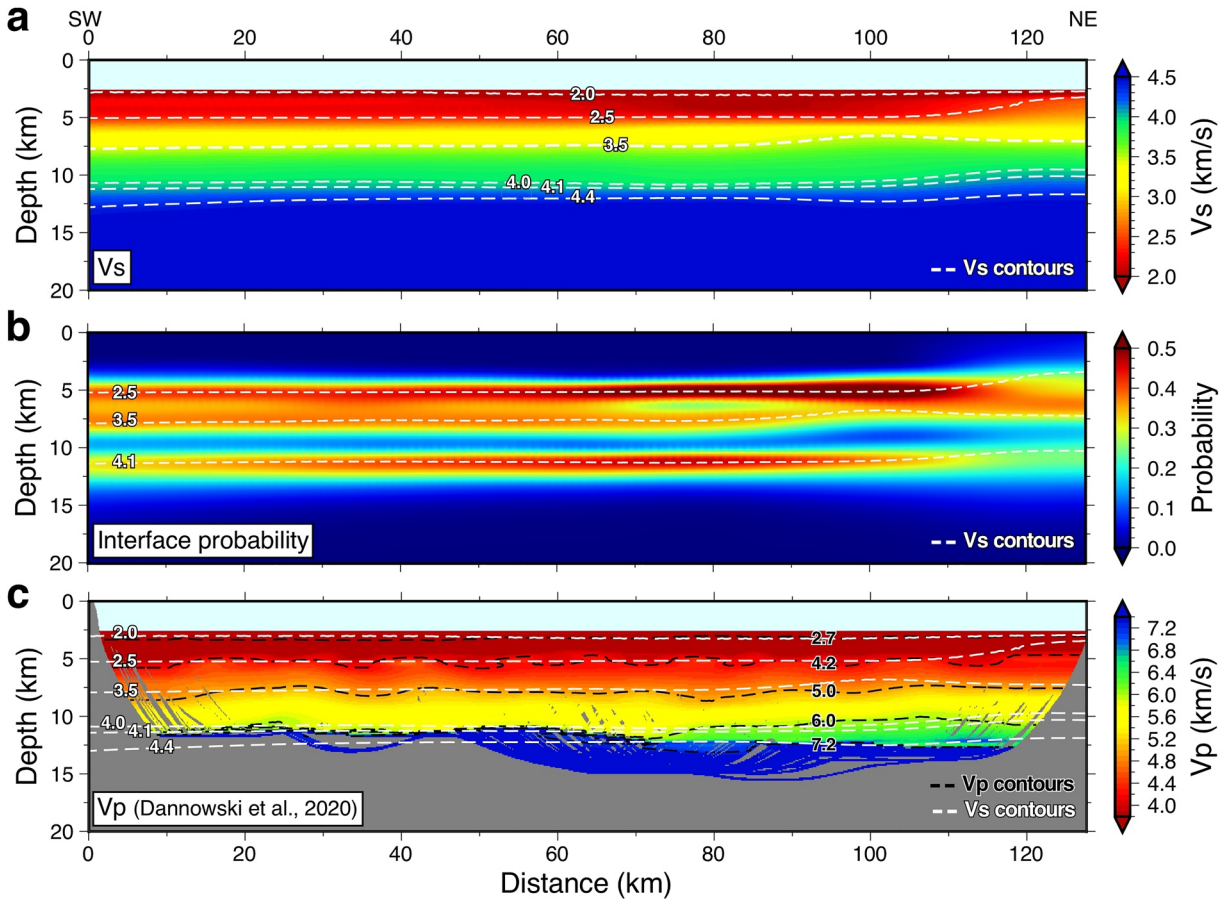

Figure 9. Depth sections along the LOBSTER-P02 transect (location shown in Figure 8a). (a) Shear-wave velocities from our final model. The 2, 2.5, 3.5, 4, 4.1, and 4.4 km/s V_s contours are shown as white dashed lines. The water column is in sky blue. (b) Posterior probability densities of presence of a layer boundary obtained from the Bayesian inversion. White dashed lines indicate the 2.5, 3.5 and 4.1 km/s V_s contours. (c) *P*-wave velocities from Dannowski et al. (2020). Black dashed lines indicate the 2.7, 4.2, 5, 6, and 7.2 km/s V_p contours; white dashed lines as in (a).

These *P*- and *S*-wave velocities are typical of gabbro (Grevemeyer et al., 2018), which suggests a gabbro intrusive body within the oceanic crust. Our interpretation is at odd with Dannowski et al. (2020) who interpreted the high V_p part of the deep crust as hyper-extended continental crust based on gravity modeling. The observed high *S*-wave velocity rules out the continental crust hypothesis.

As outlined by Dannowski et al. (2020), the $V_p = 7.2$ km/s is a good Moho proxy because it coincides with a very strong velocity gradient. In the southwestern part of the profile ($x < 70$ km), the $V_p = 7.2$ km/s contour closely corresponds to the $V_s = 4.1$ km/s contour while it corresponds to the $V_s = 4.4$ km/s contour for $x > 70$ km, that is beneath the gabbroic intrusion (Figure 9c). Owing to the presence of the gabbro intrusion, a single *S*-wave velocity contour cannot be used as proxy for the petrological Moho in the Ligurian-Provence basin, unlike in continental areas (Nouibat et al., 2022).

In the southwestern part of the profile, the depths of the V_s (4.1 km/s) and V_p (7.2 km/s) Moho proxies differ by less than 1 km. Such a small discrepancy is remarkable, given that the two models are totally independent. The depth profiles of the two shallower layer boundaries are also remarkably similar to those of the V_p contours that define lithological layering in the western Mediterranean basins (Figure 8b). Such similarity to the *P*-wave velocity model of Dannowski et al. (2020) validates the offshore part of our shear-wave velocity model, as similarity to the receiver function section of the Cifalps profile validated its onshore part (Nouibat et al., 2022).

In the few locations where information on *P*-wave velocity is available, the uppermost mantle has the seismic signature of a dry peridotite, with $V_p > 7.2$ km/s and $V_s > 4.0$ km/s (Grevemeyer et al., 2018). We find no evidence

of serpentinized mantle, which would show much lower *P*- and *S*-wave velocities. Dannowski et al. (2020) and Wolf et al. (2021) also concluded on low mantle serpentinization in this part of the basin axis.

6. Conclusion

Using data of 23 OBS of the AlpArray network with those of 890 temporary and permanent onshore stations, we have derived a 3-D high-resolution shear-wave velocity model encompassing the Ligurian-Provence basin and its conjugate margins. The OBS continuous records could be fully exploited after a careful, specific pre-processing scheme including removal of instrument noises (glitches) and reduction of seabed-induced compliance and tilt noises. We enhanced the quality of correlations between OBSs and maximized the path coverage in the Ligurian-Provence basin by involving correlations with onshore stations to virtually reconstruct Rayleigh waves propagating between OBSs. As in Nouibat et al. (2022), we computed 2-D group-velocity maps and their uncertainties using a data-driven transdimensional inversion of Rayleigh-wave group-velocity measurements. The dispersion data and their uncertainties have then been used jointly in a Bayesian probabilistic approach to derive a 3-D probabilistic shear-wave velocity model. The output average model was further refined using a linear inversion that accounts for the presence of the water column.

The comparison with the high-resolution *P*-wave velocity section derived by Dannowski et al. (2020) from travel time inversion of controlled-source seismic data along the basin axis validates our 3-D ANT model. Layer boundaries revealed by high probabilities of presence of an interface and V_s contours are remarkably consistent with V_p contours. The joint interpretation of the V_p and V_s models highlights a relatively thin anomalous oceanic crust of low *P*-wave velocities but rather high *S*-wave velocities. In the NE part of the profile, the lower part of the crust exhibits a gabbroic intrusive body. The underlying mantle is anhydrous and shows no evidence of serpentinization. These results show the potential of a joint interpretation of V_p and V_s models since they provide reliable answers to a number of debated questions on the petrological nature of the crust and uppermost mantle of the Ligurian-Provence basin, at least along the LOBSTER-P02 seismic profile. They also warrant the same type of study on the SEFASILS controlled-source seismic profile that crosses the northern margin of the basin (Dessa et al., 2020).

The use of OBS recordings in ambient-noise tomography is more challenging than with onshore stations due to shorter recording times, a higher potential of technical problems, sea-floor noises and generally a poorer SNR in the frequency bands of microseismic noise that are key for ambient-noise tomography. Parts of these problems have been solved here by a specific pre-processing of OBS records that reduces instrument and sea-floor generated noises such as tilt and compliance. When available, land stations can be used in combination with OBSs to provide higher quality surface-wave signals between offshore and onshore stations than for OBS pairs, therefore improving interstation path coverage of ANT in particular at the ocean-continent transition. We went a step further by showing how to take full benefit of onshore stations to enhance the quality of correlations for OBS pairs. Our Rayleigh-wave reconstruction scheme for OBS pairs based on second-order correlations between OBSs and land stations has proven to be effective in improving the coverage of the offshore domain. Finally, the transdimensional inversion of the enhanced set of Rayleigh-wave group-velocity observations for group-velocity maps and their uncertainties and the following hybrid inversion for V_s that accounts for the water layer have lead to a high-quality 3-D V_s model of the study region. We have therefore set up a complete, efficient and reliable ambient-noise imaging methodology of oceanic domains and their margins using OBSs and land stations that opens new perspectives for the processing of similar datasets.

Appendix A

CIFALPS Team

Coralie Aubert, Elena Eva, Stéphane Guillot, Marco G. Malusa, Silvia Pondrelli, Simone Salimbeni, Stefano Solarino, Liang Zhao.

AlpArray Team

György Hetényi, Rafael Abreu, Ivo Allegretti, Maria-Theresia Apoloner, Coralie Aubert, Simon Besançon, Maxime Bès de Berc, Götz Bokelmann, Didier Brunel, Marco Capello, Martina Čarman, Adriano Cavaliere,

Jérôme Chèze, Claudio Chiarabba, John Clinton, Glenn Cougoulat, Wayne C. Crawford, Luigia Cristiano, Tibor Czifra, Ezio D'Alema, Stefania Danesi, Romuald Daniel, Anke Dannowski, Iva Dasović, Anne Deschamps, Jean-Xavier Dessa, Cécile Doubre, Sven Egdorf, ETHZ-SED Electronics Lab, Tomislav Fiket, Kasper Fischer, Wolfgang Friederich, Florian Fuchs, Sigward Funke, Domenico Giardini, Aladino Govoni, Zoltán Gráczer, Gidera Gröschl, Stefan Heimers, Ben Heit, Davorka Herak, Marijan Herak, Johann Huber, Dejan Jarić, Petr Jedlička, Yan Jia, Hélène Jund, Edi Kissling, Stefan Klingen, Bernhard Klotz, Petr Kolínský, Heidrun Kopp, Michael Korn, Josef Kotek, Lothar Kühne, Krešo Kuk, Dietrich Lange, Jürgen Loos, Sara Lovati, Deny Malengros, Lucia Margheriti, Christophe Maron, Xavier Martin, Marco Massa, Francesco Mazzarini, Thomas Meier, Laurent Métral, Irene Molinari, Milena Moretti, Anna Nardi, Jurij Pahor, Anne Paul, Catherine Péquegnat, Daniel Petersen, Damiano Pesaresi, Davide Piccinini, Claudia Piromallo, Thomas Plenefisch, Jaroslava Plomerová, Silvia Pondrelli, Snježan Prevolnik, Roman Racine, Marc Régnier, Miriam Reiss, Joachim Ritter, Georg Rümpker, Simone Salimbeni, Marco Santulin, Werner Scherer, Sven Schippkus, Detlef Schulte-Kortnack, Vesna Šipka, Stefano Solarino, Daniele Spallarossa, Kathrin Spieker, Josip Stipčević, Angelo Strollo, Bálint Süle, Gyöngyvér Szanyi, Eszter Szűcs, Christine Thomas, Martin Thorwart, Frederik Tilmann, Stefan Ueding, Massimiliano Vallocchia, Luděk Vecsey, René Voigt, Joachim Wassermann, Zoltán Wéber, Christian Weidle, Viktor Wesztergom, Gauthier Weyland, Stefan Wiemer, Felix Wolf, David Wolyniec, Thomas Zieke, Mladen Živčić, Helena Žlebčíková.

Acknowledgments
This study was partly funded by the SEISCOPE consortium (https://seiscope2.osug.fr), sponsored by AKERBP, CGG, CHEVRON, EQUINOR, EXXON-MOBIL, JGI, SHELL, SINOPEC, SISPROBE and TOTAL, and by the RGF program (Référentiel Géologique de la France, http://rgf.brgm.fr/). It is part of the AlpArray-FR project funded by Agence Nationale de la Recherche (contract ANR-15-CE31-0015) and by Labex OSUG@2020 (Investissements d'Avenir, ANR-10-LABX-56). The deployment of OBSs for 8 months in the Liguro-Provençal basin was funded by project AlpArray-FR for the French component, and by the LOBSTER project that is part of the German Priority Programme SPP2017 4D-MB for the German component. This study was granted access to the HPC resources of the Dahu platform of the CIMENT infrastructure (https://gricad.univ-grenoble-alpes.fr/), which is supported by the Auvergne-Rhône-Alpes region (grant CPER07-13CIRA), the Labex OSUG@2020 (reference ANR10 LABX56) and the Equip@Meso project (reference ANR-10-EQPX-29-01) of the program "Investissements d'Avenir" supervised by the Agence Nationale de la Recherche and the HPC resources of CINES/IDRIS/TGCC under allocation 046091 by GENCI. We warmly thank Aurélien Mordret for his constructive feedback on our inversion methodology and Anke Dannowski for providing us the P-wave velocity model. We are grateful to the operators of European permanent seismic networks who make their data available through EIDA (http://www.orfeus-eu.org/data/eida/). We are grateful to the captains and crews of R.V. Pourquoi Pas? (France) and R.V. Maria S. Merian (Germany) for their work during the AlpArray-Leg-1 deployment cruise (https://doi.org/10.17600/17000400) and the MSM71-LOBSTER recovery cruise (https://doi.org/10.3289/GEOMAR_REP_NS_41_2018). We also thank all members of the scientific crews, in particular C. Aubert, S. Besançon and R. Daniel. The DEPAS pool provided 16 sea-bottom instruments used in his work, while the INSU-IPGP pool provided 7 broadband OBSs.

Data Availability Statement

Our tomographic 3-D model will be available in the Résif products repository (Réseau sismologique et géodésique Français; https://www.resif.fr/en/data-and-products/products-repository/). The inversion code is available on request to the first author. Waveform data used in this paper are available through the EIDA (European Integrated Data Archive) service of ORFEUS (http://www.orfeus-eu.org/eida/) and belong to the permanent networks with codes AC, BE (Royal Observatory of Belgium, 1985), CA (Institut Cartogràfic I Geològic De Catalunya: Institut D'Estudis Catalans, 1984), CH (Swiss Seismological Service [SED] At ETH Zurich, 1983), CR (University of Zagreb, 2001), CZ (Institute of Geophysics of The Academy of Sciences of The Czech Republic, 1973), ES (Instituto Geografico Nacional, Spain, 1999), FR (RESIF, 1995), G (Institut de Physique du Globe de Paris [IPGP] & Ecole et Observatoire des Sciences de la Terre de Strasbourg [EOST], 1982), GB (GEOFON Data Centre, 1993), GR (Federal Institute for Geosciences & Natural Resources [BGR], 1976), IV (INGV Seismological Data Centre, 2006), NL (KNMI, 1993), OE (ZAMG-Zentralanstalt Für Meterologie Und Geodynamik, 1987), SL (Slovenian Environment Agency, 2001), and UP (SNSN, 1904). We also used data of the temporary AlpArray network (network code Z3, AlpArray Seismic Network, 2015), Cifalps-2 experiments (network code XT, Zhao et al., 2018) and EASI experiments (network code XT, AlpArray Seismic Network, 2014).

References

Alder, C., Debayle, E., Bodin, T., Paul, A., Stehly, L., & Pedersen, H., & The AlpArray Working Group. (2021). Evidence for radial anisotropy in the lower crust of the Apennines from Bayesian ambient noise tomography in Europe. *Geophysical Journal International*, *226*(2), 941–967. https://doi.org/10.1093/gji/ggab066

AlpArray Seismic Network. (2014). *Eastern Alpine Seismic Investigation (EASI)—AlpArray Complimentary Experiment*. AlpArray Working Group. https://doi.org/10.12686/alparray/xt_2014

AlpArray Seismic Network. (2015). *AlpArray Seismic Network (AASN) temporary component*. AlpArray Working Group. https://doi.org/10.12686/ALPARRAY/Z3_2015

Batsi, E., Tsang-Hin-Sun, E., Klingelhoefer, F., Bayrakci, G., Chang, E. T., Lin, J.-Y., et al. (2019). Nonseismic signals in the ocean: Indicators of deep sea and seafloor processes on ocean-bottom seismometer data. *Geochemistry, Geophysics, Geosystems*, *20*(8), 3882–3900. https://doi.org/10.1029/2019GC008349

Bayer, R., Le Mouel, J., & Le Pichon, X. (1973). Magnetic anomaly pattern in the western Mediterranean. *Earth and Planetary Science Letters*, *19*(2), 168–176. https://doi.org/10.1016/0012-821x(73)90111-8

Bellon, H. (1981). Chronologie radiométrique (K-Ar) des manifestations magmatiques autour de la Méditerranée occidentale entre 33 et 1 Ma. In *Consiglio nazionale delle ricerche. International Conference* (pp. 341–360).

Beslier, M.-O., Ask, M., & Boillot, G. (1993). Ocean-continent boundary in the Iberia Abyssal Plain from multichannel seismic data. *Tectonophysics*, *218*(4), 383–393. https://doi.org/10.1016/0040-1951(93)90327-g

Bodin, T., Sambridge, M., Rawlinson, N., & Arroucau, P. (2012). Transdimensional tomography with unknown data noise. *Geophysical Journal International*, *189*(3), 1536–1556. https://doi.org/10.1111/j.1365-246X.2012.05414.x

Boillot, G., Féraud, G., Recq, M., & Girardeau, J. (1989). Undercrusting by serpentinite beneath rifted margins. *Nature*, *341*(6242), 523–525. https://doi.org/10.1038/341523a0

Bonatti, E., Seyler, M., Channell, J., Girardeau, J., & Mascle, G. (1990). Peridotites drilled from the Tyrrhenian Sea, ODP LEG 107. In *Proceedings of the Ocean Drilling Program Scientific results* (Vol. 107, pp. 37–47).

Bullock, A. D., & Minshull, T. A. (2005). From continental extension to seafloor spreading: Crustal structure of the Goban Spur rifted margin, southwest of the UK. *Geophysical Journal International*, *163*(2), 527–546. https://doi.org/10.1111/j.1365-246X.2005.02726.x

Coulon, C. (1977). *Le volcanisme calco-alcalin cénozoique de Sardaigne (Italie): Pétrologie, géochimie et genese des laves andésitiques et des ignimbrites: Signification géodynamique, these de doctorat*. Université d'Aix-Marseille III.

Crawford, W. (2017). AlpArray LEG1 cruise, RV Pourquoi pas? https://doi.org/10.17600/17000400

Crawford, W., & Webb, S. (2000). Identifying and removing tilt noise from low-frequency (<0.1 Hz) seafloor vertical seismic data. *Bulletin of the Seismological Society of America*, *90*(4), 952–963. https://doi.org/10.1785/0119990121

Crawford, W., Webb, S., & Hildebrand, J. (1998). Estimating shear velocities in the oceanic crust from compliance measurements by two-dimensional finite difference modeling. *Journal of Geophysical Research*, *103*(B5), 9895–9916. https://doi.org/10.1029/97JB03532

Dannowski, A., Kopp, H., Grevemeyer, I., Lange, D., Thorwart, M., Bialas, J., & Wollatz-Vogt, M. (2020). Seismic evidence for failed rifting in the Ligurian Basin, Western Alpine domain. *Solid Earth*, *11*(3), 873–887. https://doi.org/10.5194/se-11-873-2020

Deen, M., Wielandt, E., Stutzmann, E., Crawford, W., Barruol, G., & Sigloch, K. (2017). First observation of the Earth's permanent free oscillations on ocean bottom seismometers. *Geophysical Research Letters*, *44*(21), 10988–10996. https://doi.org/10.1002/2017GL074892

Dessa, J.-X., Beslier, M.-O., Schenini, L., Chamot-Rooke, N., Corradi, N., Delescluse, M., et al. (2020). Seismic exploration of the deep structure and seismogenic faults in the Ligurian Sea by joint multi channel and ocean bottom seismic acquisitions: Preliminary results of the SEFASILS cruise. *Geosciences*, *10*(3), 108. https://doi.org/10.3390/geosciences10030108

Déverchère, J., & Beslier, M.-O. (1995). Malis cruise, rv le nadir. https://doi.org/10.17600/95000010

de Verdière, Y. C. (2006). Mathematical models for passive imaging I: General background. arXiv: Mathematical Physics.

Dziewonski, A., & Anderson, L. (1981). Preliminary reference Earth model. *Physics of the Earth and Planetary Interiors*, *25*(4), 297–356. https://doi.org/10.1016/0031-9201(81)90046-7

Dziewonski, A., Bloch, S., & Landisman, M. (1969). A technique for the analysis of transient seismic signals. *Bulletin of the Seismological Society of America*, *59*(1), 427–444. https://doi.org/10.1785/bssa0590010427

Egger, A., Demartin, M., Ansorge, J., Banda, E., & Maistrello, M. (1988). The gross structure of the crust under Corsica and Sardinia. *Tectonophysics*, *150*(3), 363–389. https://doi.org/10.1016/0040-1951(88)90075-3

Faccenna, C., Becker, T. W., Auer, L., Billi, A., Boschi, L., Brun, J. P., et al. (2014). Mantle dynamics in the Mediterranean. *Reviews of Geophysics*, *52*(3), 283–332. https://doi.org/10.1002/2013RG000444

Faccenna, C., Mattei, M., Funiciello, R., & Jolivet, L. (1997). Styles of back-arc extension in the central Mediterranean. *Terra Nova*, *9*(3), 126–130. https://doi.org/10.1046/j.1365-3121.1997.d01-12.x

Federal Institute for Geosciences, & Natural Resources (BGR). (1976). *German Regional Seismic Network (GRSN)*. Federal Institute for Geosciences and Natural Resources (BGR). https://doi.org/10.25928/MBX6-HR74

Gailler, A., Klingelhoefer, F., Olivet, J.-L., Aslanian, D., & Technical, O. (2009). Crustal structure of a young margin pair: New results across the Liguro–Provencal Basin from wide-angle seismic tomography. *Earth and Planetary Science Letters*, *286*(1–2), 333–345. https://doi.org/10.1016/j.epsl.2009.07.001

GEOFON Data Centre. (1993). *GEOFON seismic network*. Deutsches GeoForschungsZentrum GFZ. https://doi.org/10.14470/TR560404

Grevemeyer, I., Hayman, N. W., Peirce, C., Schwardt, M., Van Avendonk, H. J., Dannowski, A., & Papenberg, C. (2018). Episodic magmatism and serpentinized mantle exhumation at an ultraslow-spreading centre. *Nature Geoscience*, *11*(6), 444–448. https://doi.org/10.1038/s41561-018-0124-6

Gueguen, E., Doglioni, C., & Fernandez, M. (1998). On the post-25 Ma geodynamic evolution of the western Mediterranean. *Tectonophysics*, *298*(1), 259–269. https://doi.org/10.1016/S0040-1951(98)00189-9

Hable, S., Sigloch, K., Barruol, G., Stähler, S. C., & Hadziioannou, C. (2018). Clock errors in land and ocean bottom seismograms: High-accuracy estimates from multiple-component noise cross-correlations. *Geophysical Journal International*, *214*(3), 2014–2034. https://doi.org/10.1093/gji/ggy236

Hable, S., Sigloch, K., Stutzmann, E., Kiselev, S., & Barruol, G. (2019). Tomography of crust and lithosphere in the western Indian Ocean from noise cross-correlations of land and ocean bottom seismometers. *Geophysical Journal International*, *219*(2), 924–944. https://doi.org/10.1093/gji/ggz333

Harmon, N., Forsyth, D., & Webb, S. (2007). Using ambient seismic noise to determine short-period phase velocities and shallow shear velocities in young oceanic lithosphere. *Bulletin of the Seismological Society of America*, *97*(6), 2009–2023. https://doi.org/10.1785/0120070050

Herrmann, R. B. (1973). Some aspects of band-pass filtering of surface waves. *Bulletin of the Seismological Society of America*, *63*(2), 663–671. https://doi.org/10.1785/BSSA0630020663

Herrmann, R. B. (2013). Computer programs in seismology: An evolving tool for instruction and research. *Seismological Research Letters*, *84*(6), 1081–1088. https://doi.org/10.1785/0220110096

Hetényi, G., Molinari, I., Clinton, J., Bokelmann, G., Bondar, I., Crawford, W. C., et al. (2018). The AlpArray seismic network: A large-scale European experiment to image the Alpine orogen. *Surveys in Geophysics*, *39*(5), 1009–1033. https://doi.org/10.1007/s10712-018-9472-4

INGV Seismological Data Centre. (2006). *Rete Sismica Nazionale (RSN)*. Istituto Nazionale di Geofisica e Vulcanologia (INGV). https://doi.org/10.13127/SD/X0FXNH7QFY

Institut Cartogràfic I Geològic De Catalunya: Institut D'Estudis Catalans. (1984). *Catalan seismic network*. International Federation of Digital Seismograph Networks. https://doi.org/10.7914/SN/CA

Institut de Physique du Globe de Paris (IPGP) and Ecole et Observatoire des Sciences de la Terre de Strasbourg (EOST). (1982). *GEOSCOPE, French Global Network of broad band seismic stations*. Institut de Physique du Globe de Paris (IPGP). https://doi.org/10.18715/GEOSCOPE.G

Institute of Geophysics of the Academy of Sciences of the Czech Republic. (1973). *Czech Regional Seismic Network*. International Federation of Digital Seismograph Networks. https://doi.org/10.7914/SN/CZ

Instituto Geografico Nacional, Spain. (1999). *Spanish Digital Seismic Network. International Federation of Digital Seismograph Networks*. International Federation of Digital Seismograph Networks. https://doi.org/10.7914/SN/ES

Jolivet, L., Romagny, A., Gorini, C., Maillard, A., Thinon, I., Couëffé, R., et al. (2020). Fast dismantling of a mountain belt by mantle flow: Late-orogenic evolution of Pyrenees and Liguro-Provençal rifting. *Tectonophysics*, *776*, 228312. https://doi.org/10.1016/j.tecto.2019.228312

Klingelhoefer, F., Olivet, J., Aslanian, D., Bache, F., Moulin, M., Matias, L., et al. (2008). Preliminary results from the Sardinia deep seismic cruise on the Western Sardinia and Gulf of Lions conjugate margin pair. In *EGU Meeting April 2008*.

KNMI. (1993). *Netherlands Seismic and Acoustic Network*. Royal Netherlands Meteorological Institute (KNMI). https://doi.org/10.21944/e970fd34-23b9-3411-b366-e4f72877d2c5

Kopp, H., Lange, D., Thorwart, M., Paul, A., Dannowski, A., Petersen, F., et al. (2018). RV MARIA S. MERIAN Fahrtbericht/Cruise Report MSM71 LOBSTER: Ligurian Ocean Bottom Seismology and Tectonics Research, Las Palmas (Spain)–Heraklion (Greece) 07.02.–27.02.2018.

Kvapil, J., Plomerová, J., Kampfová Exnerová, H., Babuška, V., Hetényi, G., & Group, A. W. (2021). Transversely isotropic lower crust of Variscan central Europe imaged by ambient noise tomography of the Bohemian Massif. *Solid Earth*, *12*(5), 1051–1074. https://doi.org/10.5194/se-12-1051-2021

Leprêtre, A., Klingelhoefer, F., Graindorge, D., Schnurle, P., Beslier, M.-O., Yelles, K., et al. (2013). Multiphased tectonic evolution of the Central Algerian margin from combined wide-angle and reflection seismic data off Tipaza, Algeria. *Journal of Geophysical Research: Solid Earth*, *118*(8), 3899–3916. https://doi.org/10.1002/jgrb.50318

Levander, A., Schmandt, B., Miller, M. S., Liu, K., Karlstrom, K. E., Crow, R. S., et al. (2011). Continuing Colorado plateau uplift by delamination-style convective lithospheric downwelling. *Nature*, *472*(7344), 461–465. https://doi.org/10.1038/nature10001

Levshin, A., Yanovskaya, T., Lander, A., Bukchin, B., Barmin, M., Its, E., & Ratnikova, L. (1989). *Seismic Surface Waves in a Laterally Inhomogeneous Earth (Ed. V. E. Keilis-Borok)* (pp. 129–182). Kluwer Publishers.

Lobkis, O. I., & Weaver, R. L. (2001). On the emergence of the green's function in the correlations of a diffuse field. *Journal of the Acoustical Society of America*, *110*(6), 3011–3017. https://doi.org/10.1121/1.1417528

Lu, Y., Stehly, L., Brossier, R., & Paul, A., & AlpArray Working Group. (2020). Imaging Alpine crust using ambient noise wave-equation tomography. *Geophysical Journal International*, *222*(1), 69–85. https://doi.org/10.1093/gji/ggaa145

Lu, Y., Stehly, L., & Paul, A., & AlpArray Working Group. (2018). High-resolution surface wave tomography of the European crust and uppermost mantle from ambient seismic noise. *Geophysical Journal International*, *214*(2), 1136–1150. https://doi.org/10.1093/gji/ggy188

Malusà, M. G., Guillot, S., Zhao, L., Paul, A., Solarino, S., Dumont, T., et al. (2021). The deep structure of the alps based on the CIFALPS seismic experiment: A synthesis. *Geochemistry, Geophysics, Geosystems*, *22*(3), e2020GC009466. https://doi.org/10.1029/2020GC009466

Mascle, J., & Rehault, J.-P. (1990). A revised seismic stratigraphy of the Tyrrhenian Sea: Implications for the basin evolution (pp. 617–637).

McKenzie, D. (1978). Some remarks on the development of sedimentary basins. *Earth and Planetary Science Letters*, *40*(1), 25–32. https://doi.org/10.1016/0012-821x(78)90071-7

Moschetti, M. P., Ritzwoller, M. H., Lin, F., & Yang, Y. (2010). Seismic evidence for widespread western-US deep-crustal deformation caused by extension. *Nature*, *464*(7290), 885–889. https://doi.org/10.1038/nature08951

Nouibat, A., Stehly, L., Paul, A., Schwartz, S., Bodin, T., Dumont, T., et al. (2022). Lithospheric transdimensional ambient-noise tomography of W-Europe: Implications for crustal-scale geometry of the W-Alps. *Geophysical Journal International*, *229*(2), 862–879. https://doi.org/10.1093/gji/ggab520

Pascal, G., Mauffret, A., & Patriat, P. (1993). The ocean-continent boundary in the gulf of lion from analysis of expanding spread profiles and gravity modelling. *Geophysical Journal International*, *113*(3), 701–726. https://doi.org/10.1111/j.1365-246x.1993.tb04662.x

Peterson, J. R. (1993). *Observations and modeling of seismic background noise*. (Tech. Rep.). US Geological Survey.

Réhault, J.-P., Boillot, G., & Mauffret, A. (1984). The western Mediterranean basin geological evolution. *Marine Geology*, *55*(3), 447–477. (Geological and Geodynamical Aspects on the Mediterranean). https://doi.org/10.1016/0025-3227(84)90081-1

Réhault, J.-P., Honthaas, C., Guennoc, P., Bellon, H., Ruffet, G., Cotten, J., et al. (2012). Offshore Oligo-Miocene volcanic fields within the Corsica-Liguria Basin: Magmatic diversity and slab evolution in the western Mediterranean Sea. *Journal of Geodynamics*, *58*, 73–95. https://doi.org/10.1016/j.jog.2012.02.003

RESIF. (1995). RESIF-RLBP French Broad-band network, RESIF-RAP strong motion network and other seismic stations in metropolitan France. https://doi.org/10.15778/resif.fr

Reynard, B. (2013). Serpentine in active subduction zones. *Lithos*, *178*, 171–185. https://doi.org/10.1016/j.lithos.2012.10.012

Rollet, N., Déverchère, J., Beslier, M.-O., Guennoc, P., Réhault, J.-P., Sosson, M., & Truffert, C. (2002). Back arc extension, tectonic inheritance, and volcanism in the Ligurian Sea, Western Mediterranean. *Tectonics*, *21*(3), 6-1–6-23. https://doi.org/10.1029/2001TC900027

Roux, P., Sabra, K. G., Gerstoft, P., Kuperman, W., & Fehler, M. C. (2005). P-waves from cross-correlation of seismic noise. *Geophysical Research Letters*, *32*(19). https://doi.org/10.1029/2005gl023803

Royal Observatory of Belgium. (1985). *Belgian Seismic Network*. International Federation of Digital Seismograph Networks. https://doi.org/10.7914/SN/BE

Sadeghi-Bagherabadi, A., Vuan, A., Aoudia, A., Parolai, S., & The AlpArray and AlpArray-Swath-D Working Group. (2021). High-resolution crustal s-wave velocity model and Moho geometry beneath the Southeastern Alps: New insights from the SWATH-D experiment. *Frontiers of Earth Science*, *9*, 188. https://doi.org/10.3389/feart.2021.641113

Sandwell, D. T., & Smith, W. H. (1997). Marine gravity anomaly from Geosat and ERS 1 satellite altimetry. *Journal of Geophysical Research*, *102*(B5), 10039–10054. https://doi.org/10.1029/96jb03223

Sandwell, D. T., Yale, M., & Smith, W. (1995). Gravity anomaly profiles from ERS-1, Topex and Geosat altimetry. *Eos: Transactions American Geophysical Union*, *76*(17), S89.

Schippkus, S., Zigone, D., & Bokelmann, G., & The AlpArray Working Group. (2018). Ambient-noise tomography of the wider Vienna Basin region. *Geophysical Journal International*, *215*(1), 102–117. https://doi.org/10.1093/gji/ggy259

Séranne, M. (1999). The Gulf of Lion continental margin (NW Mediterranean) revisited by IBS: An overview. *Geological Society, London, Special Publications*, *156*(1), 15–36. https://doi.org/10.1144/GSL.SP.1999.156.01.03

Shapiro, N. M., & Singh, S. K. (1999). A systematic error in estimating surface-wave group-velocity dispersion curves and a procedure for its correction. *Bulletin of the Seismological Society of America*, *89*(4), 1138–1142.

Slovenian Environment Agency. (2001). *Seismic Network of the Republic of Slovenia*. International Federation of Digital Seismograph Networks. https://doi.org/10.7914/SN/SL

Snieder, R. (2004). Extracting the green's function from the correlation of coda waves: A derivation based on stationary phase. *Physical Review E*, *69*(4), 046610. https://doi.org/10.1103/physreve.69.046610

SNSN. (1904). *Swedish National Seismic Network*. Uppsala University. https://doi.org/10.18159/SNSN

Soergel, D., Pedersen, H. A., Stehly, L., Margerin, L., & Paul, A., & AlpArray Working Group. (2020). Coda-Q in the 2.5–20 s period band from seismic noise: Application to the greater Alpine area. *Geophysical Journal International*, *220*(1), 202–217. https://doi.org/10.1093/gji/ggz443

Swiss Seismological Service (SED) at ETH Zurich. (1983). *National Seismic Networks of Switzerland*. ETH Zürich. https://doi.org/10.12686/SED/NETWORKS/CH

Takeo, A., Kawakatsu, H., Isse, T., Nishida, K., Sugioka, H., Ito, A., et al. (2016). Seismic azimuthal anisotropy in the oceanic lithosphere and asthenosphere from broadband surface wave analysis of OBS array records at 60 Ma seafloor. *Journal of Geophysical Research: Solid Earth*, *121*(3), 1927–1947. https://doi.org/10.1002/2015jb012429

University of Zagreb. (2001). *Croatian Seismograph Network*. International Federation of Digital Seismograph Networks. https://doi.org/10.7914/SN/CR

van Hinsbergen, D. J., Torsvik, T. H., Schmid, S. M., Maţenco, L. C., Maffione, M., Vissers, R. L., et al. (2020). Orogenic architecture of the Mediterranean region and kinematic reconstruction of its tectonic evolution since the Triassic. *Gondwana Research*, *81*, 79–229. https://doi.org/10.1016/j.gr.2019.07.009

Wapenaar, K. (2004). Retrieving the elastodynamic Green's function of an arbitrary inhomogeneous medium by cross correlation. *Physical Review Letters*, *93*(25), 254301. https://doi.org/10.1103/PhysRevLett.93.254301

Weaver, R. L. (2005). Information from seismic noise. *Science*, *307*(5715), 1568–1569. https://doi.org/10.1126/science.1109834

Wolf, F. N., Lange, D., Dannowski, A., Thorwart, M., Crawford, W., Wiesenberg, L., et al. (2021). 3D crustal structure of the Ligurian Basin revealed by surface wave tomography using ocean bottom seismometer data. *Solid Earth*, *12*(11), 2597–2613. https://doi.org/10.5194/se-12-2597-2021

Yan, F., Han, D.-H., Yao, Q., & Chen, X.-L. (2016). Seismic velocities of halite salt: Anisotropy, heterogeneity, dispersion, temperature, and pressure effects. *Geophysics*, *81*(4), D293–D301. https://doi.org/10.1190/geo2015-0476.1

ZAMG-Zentralanstalt Für Meterologie Und Geodynamik. (1987). *Austrian Seismic Network*. International Federation of Digital Seismograph Networks. https://doi.org/10.7914/SN/OE

Zhao, L., Malusà, M. G., Yuan, H., Paul, A., Guillot, S., Lu, Y., et al. (2020). Evidence for a serpentinized plate interface favouring continental subduction. *Nature Communications*, *11*(1), 2171. https://doi.org/10.1038/s41467-020-15904-7

Zhao, L., Paul, A., & Solarino, S., & RESIF. (2018). Seismic network XT: CIFALPS temporary experiment (China-Italy-France Alps seismic transect) [Dataset]. RESIF (Réseau Sismologique et géodésique Français). https://doi.org/10.15778/RESIF.XT2018